

Comparative study of phase-field damage models for hydrogen assisted cracking

Tushar Kanti Mandal^b, Vinh Phu Nguyen^b, Jian-Ying Wu^{a,*}

^a State Key Laboratory of Subtropical Building Science, South China University of Technology, 510641 Guangzhou, China

^b Department of Civil Engineering, Monash University, Clayton, Victoria 3800, Australia

ARTICLE INFO

Keywords:

Hydrogen assisted cracking
Hydrogen embrittlement
Phase-field theory
Damage
fracture

ABSTRACT

Hydrogen assisted cracking (HAC) usually causes premature failure of metallic materials and results in unexpected collapse of structures under the environmental exposure of hydrogen. Therefore, computational modeling of HAC is of paramount significance to quantify the adverse effects of HAC on the integrity and safety of structures. In this respect phase-field models for fracture are promising since they are able to seamlessly deal with complex crack patterns like nucleation, branching, merging and even fragmentation in a standalone framework. In this work we provide a comparative study of three frequently adopted phase-field models for hydrogen assisted cracking. Both the phase-field models for brittle fracture (e.g., the AT1/2 and WN models) and the phase-field regularized cohesive zone model (PF-CZM) are considered within the unified phase-field theory for damage and fracture, and are extended to incorporate the hydrogen enhanced decohesion mechanism. The numerical implementation of the phase-field models for HAC is also presented, with a simple scheme for calculating the gradient of the hydrostatic stress. Representative numerical examples show that, the PF-CZM with an increasing Irwin's characteristic (internal) length and the PF-CZM with a constant one are both insensitive to the regularization length scale parameter. This merit make them promising for the computational modeling of HAC.

1. Introduction

Hydrogen assisted cracking (HAC), or hydrogen embrittlement, is a form of material degradation typically for metals due to the presence of atomic hydrogen. That is, when hydrogen is present, metallic materials fail at a load level that is significantly lower compared to that a hydrogen-free material can sustain. Susceptibility to HAC is generally caused by either *internal embrittlement* such as the introduction of hydrogen during coating, forming, plating, and finishing operations, or the so-called *external embrittlement* through environmental exposure, corrosion processes, cathodic protection, etc. The result is catastrophic fracture which occurs unexpectedly, most often after many years of service. Therefore, computational modeling of HAC is of paramount significance to quantify the adverse effects of HAC on the integrity and safety of structures.

HAC generally requires localization of hydrogen atoms which can occur at trap sites such as dislocations, grain boundaries, interfaces between different phases, voids or cracks. Research to date has established that there is no single mechanism applicable to all metallic

materials plus environments. Hydrogen enhanced localized plasticity (HELP), in which hydrogen favours the mobility of dislocations which implies local plasticity even if there is a macroscopically brittle failure, and hydrogen enhanced decohesion (HEDE), in which interstitial hydrogen lowers the cohesive strength, are two viable mechanisms of embrittlement [10,37]. The HEDE mechanism has been mainly modeled using the cohesive zone model (CZM) of Barenblatt [7] with a decreasing fracture energy in the presence of hydrogen. The transport of hydrogen is modeled with a diffusion equation thus resulting in a coupled displacement-hydrogen concentration problem. Typical works are Lee and Unger [30], Sofronis and McMeeking [60], Serebrinsky et al. [58], Scheider et al. [56], Díaz et al. [15]. As cracks are treated using zero-thickness interface elements (see e.g., [73,47]), only a limited set of crack paths restricted to the inter-element boundaries is allowed. More flexible crack paths can be captured using either the embedded strong discontinuity approach [59,24,69] or the eXtended Finite Element Method (XFEM) [45,62,67]. However, applications of these numerical methods to HAC problems have not been reported. Moreover, despite recent advances in these methods, computational modeling of complex

* Corresponding author.

E-mail address: jywu@scut.edu.cn (J.-Y. Wu).

<https://doi.org/10.1016/j.tafmec.2020.102840>

Received in revised form 7 November 2020; Accepted 14 November 2020

Available online 9 December 2020

0167-8442/© 2020 Elsevier Ltd. All rights reserved.

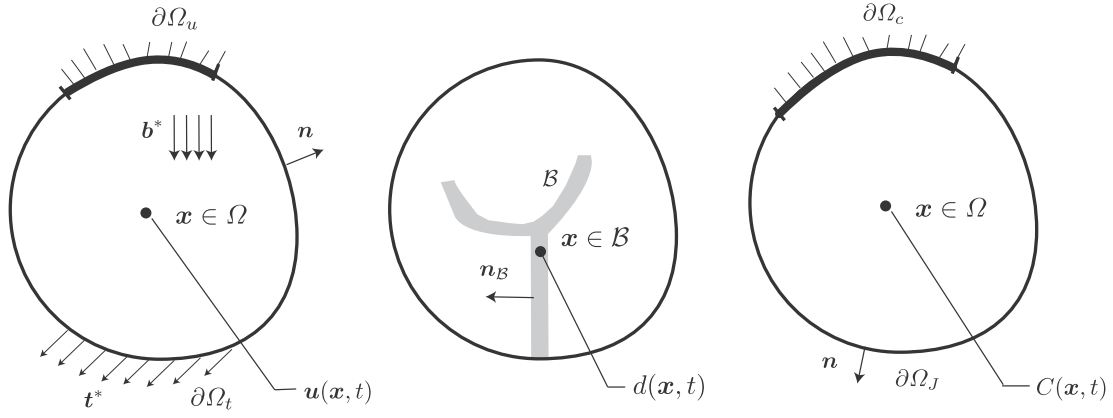


Fig. 1. Schematic of coupled displacement, hydrogen concentration and damage fields.

fracture problems that involve many intersecting cracks is, however, still an open issue especially in three-dimension.

Phase-field damage/fracture models [18,11,12] provide a promising tool to model complex two or three dimensional fracture networks over a fixed spatial discretization grid. Furthermore, there is no need to introduce *ad hoc* failure criteria that determine when/where a crack grows, how much it propagates and in which direction. In phase-field models for fracture, the sharp crack is replaced by a diffuse damage band of which the bandwidth is controlled by a length scale parameter. The cracked and the intact material is differentiated by the introduction of a scalar field referred to as the crack phase-field. They have been successfully applied to brittle fracture [50,61,21,54], cohesive fracture [63,64,68], ductile fracture [43,3], hyperelastic fracture [41,5,35], dynamic fracture [22,57,31,46,34], and multi-physics fracture [44,29,40,74]. We refer to the comprehensive reviews of phase-field damage/fracture models in Bourdin et al. [12], Wu et al. [70] for more details. Note that there are other numerical methods that can handle arbitrary crack paths, e.g., the meshfree cracking particle method [51], the dual-horizon peridynamics method [53], etc. However, in this work we focus on models/methods implemented within the finite element method which is arguably the most widely used numerical method in engineering.

Phase-field damage/fracture models have also been applied to the modeling of HAC [16,38,17,27,39,72]. Similar to aforementioned discrete approaches based on cohesive interface elements, the fracture energy is assumed to be a decreasing function of the hydrogen coverage. To understand the advantages and disadvantages of these models, the aim of this paper are twofold. First, a comparative study of several phase-field models for HAC is given within the unified phase-field theory for damage and fracture [63,64,68]. Second, details on the finite element implementation using meshes of mixed quadratic/linear elements are provided, including the calculation of the gradient of the hydrostatic stress.

The remainder of this paper is organized as follows. Within the unified phase-field theory for damage and fracture, several widely adopted phase-field damage models for HAC are presented in Section 2. Section 3 is devoted to the numerical implementation of these models in the context of multifield finite element method. In particular, a simple scheme for calculating the gradient of the hydrostatic stress is presented.

Representative examples are given in Section 4 to compare the numerical results predicted by various models. Not only the qualitative crack patterns but also the quantitative load – displacement responses are studied. The most relevant conclusions are drawn in Section 5.

Notation. Compact tensor notation is used in the theoretical part of this paper. As general rules, scalars are denoted by italic light-face Greek or Latin letters (e.g. a or λ); vectors, second- and fourth-order tensors are signified by italic boldface minuscule, majuscule and blackboard-bold majuscule characters like \mathbf{a} , \mathbf{A} and \mathbb{A} , respectively. The inner products with single and double contractions are denoted by ‘ \cdot ’ and ‘ $\cdot\cdot$ ’, respectively. Symbols with a bar on top ($\bar{\square}$) denote effective quantities whereas ones with an asterisk (\square^*) represent prescribed quantities. In the numeric part of this work, Voigt notation is adopted where vectors and second-order tensors are denoted by boldface minuscule and majuscule letters like \mathbf{a} and \mathbf{A} , respectively.

2. Phase-field damage models for hydrogen assisted cracking

In this section, various phase-field models for HAC [38,72] are presented within the framework of the unified phase-field theory for damage and fracture [63,64,68].

As shown in Fig. 1, the reference configuration of a cracking solid $\Omega \subset \mathbb{R}^{n_{\text{dim}}}$ ($n_{\text{dim}} = 1, 2, 3$) with a sharp crack set $S \subset \mathbb{R}^{n_{\text{dim}}-1}$ is considered. The external boundary is denoted by $\partial\Omega \subset \mathbb{R}^{n_{\text{dim}}-1}$, with the outward unit normal signified by vector \mathbf{n} . The material particles of the solid are labeled by their spatial coordinates \mathbf{x} .

Assume that the solid is subjected to volumetric body forces (per unit mass) \mathbf{b}^* and surface tractions \mathbf{t}^* for some part of the external boundary $\partial\Omega_c \subset \partial\Omega$. The resulting displacement field is denoted by $\mathbf{u}(\mathbf{x}) : \Omega \rightarrow \mathbb{R}^{n_{\text{dim}}}$, with the given displacements \mathbf{u}^* applied to the complementary boundary $\partial\Omega_u \subset \partial\Omega$. Upon the assumption of infinitesimal deformations, the strain field $\boldsymbol{\epsilon}(\mathbf{x}) : \Omega \rightarrow [\mathbb{R}^{n_{\text{dim}} \times n_{\text{dim}}}]^{\text{sym}}$ is given by $\boldsymbol{\epsilon}(\mathbf{x}) := \nabla^{\text{sym}} \mathbf{u}(\mathbf{x})$, for the symmetric gradient operator $\nabla^{\text{sym}}(\cdot)$ with respect to the spatial coordinates \mathbf{x} .

In the context of phase-field models for fracture, the sharp crack S is smeared over a localization band $B \subset \Omega$ in which the crack phase-field or damage field $d(\mathbf{x}) : B \rightarrow [0, 1]$ lumps, with the exterior domain $\Omega \setminus B$ being intact. The localization bandwidth is characterized by a length scale

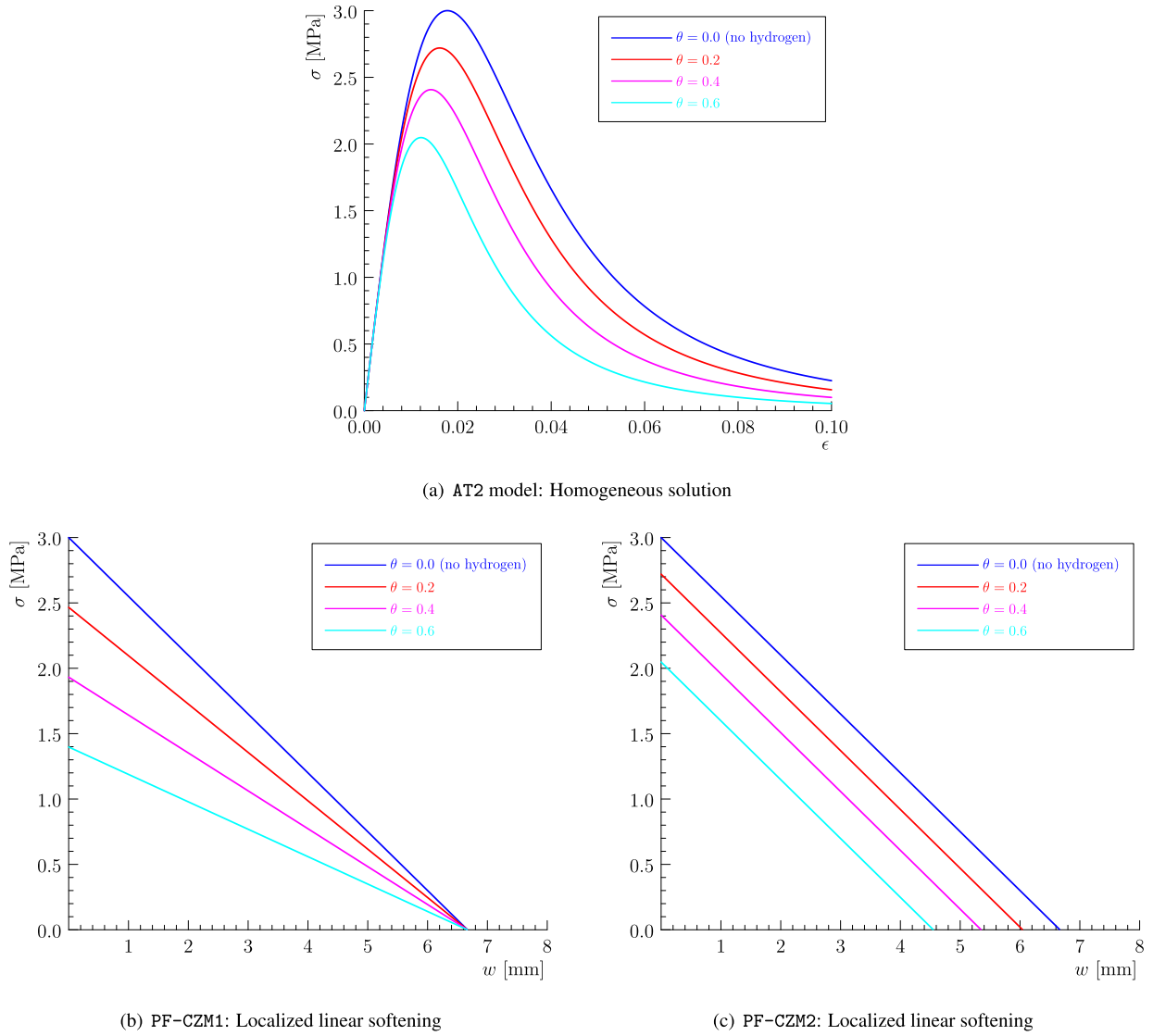


Fig. 2. Hydrogen-dependent softening laws with the degradation function (2.12): $\chi = 0.89$, $G_f = 10$ N/mm and $f_t = 3.0$ MPa.

parameter b that can be regarded either as a material property or a numerical parameter. As in the classical continuum damage mechanics, the damage field satisfies the irreversibility (i.e., the unrecoverable property excluding self-healing) $\dot{d}(x) \geq 0$, with $d(x) = 0$ implying intact material with no damage and $d(x) = 1$ representing pre-defined cracks or complete fracture.

In the presence of hydrogen diffusion, the concentration field is denoted by $C(x) : \Omega \rightarrow \mathbb{R}_+$. Similarly, the external boundary $\partial\Omega$ of the solid is decomposed into one part $\partial\Omega_C$ where the given hydrogen concentration C^* is imposed and the complementary one $\partial\Omega_J$ where the flux J^* is prescribed through the boundary.

Upon the above settings, the governing equations of phase-field models for hydrogen assisted cracking, with the displacement field $\mathbf{u}(x)$, the hydrogen concentration field $C(x)$ and the damage field $d(x)$ being the primary field variables all dependent on time t is implicitly specified., are summarized in Box 1; see Wu et al. [72].

In the above box, the effective damage driving force \bar{Y} is defined in terms of an equivalent effective stress $\bar{\sigma}_{eq}$

$$\bar{Y} := \frac{1}{2E_0} \langle \bar{\sigma}_{eq} \rangle^2 \quad (2.1)$$

for Young's modulus E_0 and Macauley brackets $\langle x \rangle = \max(x, 0)$. Regarding brittle and quasi-brittle fracture, the classical Rankine criterion can be adopted, i.e., $\bar{\sigma}_{eq} = \bar{\sigma}_1$, where $\bar{\sigma}_1$ denotes the major principal value of the effective stress tensor $\bar{\sigma} := \mathbb{E}_0 : \epsilon$, with \mathbb{E}_0 being the fourth-order elasticity tensor.

In the molar bulk chemical potential μ with the initial value μ_0 , D is the bulk diffusivity, R is the universal gas constant, T is the absolute temperature, V_H is the partial molar volume of the impurity and $\sigma_H := \frac{1}{3} \text{tr} \sigma$ is the hydrostatic (volumetric) stress.

Box 1: Phase-field models for hydrogen assisted cracking

Components	Displacement sub-problem	Hydrogen sub-problem	Damage sub-problem ^a
Governing equations	$\nabla \cdot \sigma + b^* = 0$ $\sigma \cdot n = t^*$	$\nabla \cdot J + \dot{C} = 0$ $J \cdot n = J^*$	$\nabla \cdot q + Q \leq 0$ $q \cdot n_b \geq 0$
Constitutive relations	$\sigma = \omega(d)\mathbb{E}_0 : \epsilon$ $Y = -\omega'(d)\bar{Y}$	$J = -\frac{DC}{RT}\nabla\mu$ $\mu = \mu_0 + RT \ln C - V_H\sigma_H$	$q = \frac{2b}{c_\alpha}G_f \cdot \nabla d$ $Q = Y - \frac{G_f}{c_\alpha b}\alpha'(d)$
Dirichlet bcs	$u = u^*$ on $\partial\Omega_u$	$C = C^*$ on $\partial\Omega_C$	$d = d^*$ on $\partial\Omega_d$
Initial conditions	NA	$C = C_0$	NA

^aThe damage irreversibility $\dot{d} \geq 0$ and boundedness $d \in [0, 1]$ have to be fulfilled.

2.1. Phase-field models for hydrogen assisted cracking

The (monotonically decreasing) energetic degradation function $\omega(d) \in [0, 1]$ and the (monotonically increasing) geometric crack function $\alpha(d) \in [0, 1]$ satisfy the following conditions

$$\alpha'(d) \geq 0; \quad \alpha(0) = 0, \quad \alpha(1) = 1 \quad (2.2a)$$

$$\omega'(d) \leq 0, \quad \omega'(1) = 0; \quad \omega(0) = 1, \quad \omega(1) = 0 \quad (2.2b)$$

for the first derivatives $\omega'(d) := \partial\omega/\partial d$ and $\alpha'(d) := \partial\alpha/\partial d$, respectively. The scaling coefficient $c_\alpha := 4 \int_0^1 \sqrt{\alpha(\beta)} d\beta$ is introduced to reproduce the fracture energy G_f upon complete failure.

In accordance with the unified phase-field theory for damage and fracture [63], the following generic functions are considered for brittle fracture [68]

$$\begin{cases} \alpha(d) = \xi d + (1 - \xi)d^2 \\ \omega(d) = \frac{(1 - d)^2}{(1 - d)^2 + a_1 d \left(1 - \frac{1}{2}d\right)} \end{cases} \quad (2.3)$$

where $\xi \in [0, 2]$ and $a_1 > 0$ are both parameters to be specified.

2.1.1. Phase-field models for brittle fracture

The most common phase-field model for brittle fracture employs the following quadratic degradation function

$$\omega(d) = (1 - d)^2 \quad (2.4)$$

which corresponds to the generic function (2.3)₂ with a fixed parameter $a_1 = 2$.

Regarding the crack geometric functional $\alpha(d)$, the so-called the AT2 model with $\xi = 0$ [11,12], the AT1 model with $\xi = 1$ [49], and the WN model with $\xi = 2$ [68], can be recovered for the following particular cases

$$\alpha \left(d \right) = \begin{cases} d & \text{AT1} \\ d^2 & \text{AT2} \\ 2d - d^2 & \text{WN} \end{cases} \Rightarrow c_\alpha = \begin{cases} \frac{8}{3} & \text{AT1} \\ 2 & \text{AT2} \\ \pi & \text{WN} \end{cases} \quad (2.5)$$

The corresponding critical stresses or failure strengths f_t are given by [70]

$$f_t = \begin{cases} \sqrt{\frac{3E_0 G_f}{8b}} & \text{AT1} \\ \frac{3}{16} \sqrt{\frac{3E_0 G_f}{b}} & \text{AT2} \\ \sqrt{\frac{2E_0 G_f}{\pi b}} & \text{WN} \end{cases} \quad (2.6)$$

As can be seen, the failure strength f_t is not an independent material property. Rather, it is a dependent one related to Young's modulus E_0 and fracture energy G_f , and inversely proportional to the square root of the length scale parameter b . Note that, as the elastic stage is lacking and damage nucleates from the very beginning of the applied loading, in the AT2 model the failure strength f_t is usually taken as the maximum stress regarding a softening bar under uniaxial stretching.

Accordingly, the length scale b in the AT1/2 and WN models is not a numerical parameter, but a dependent material property [49,61] as in the gradient damage models [19,32]

$$b = \begin{cases} \frac{3}{8} l_{ch} & \text{AT1} \\ \frac{27}{256} l_{ch} & \text{AT2} \\ \frac{2}{\pi} l_{ch} & \text{WN} \end{cases} \quad (2.7)$$

for Irwin's characteristic (internal) length $l_{ch} := E_0 G_f / f_t^2$.

In order to describe the hydrogen enhanced decohesion (HEDE) mechanism, the fracture energy G_f is related to the hydrogen coverage (or surface concentration) θ [58,14]

$$G_f(\theta) = \phi(\theta) G_{f0} \Rightarrow f_t = \sqrt{\phi(\theta)} f_{t0} \quad (2.8)$$

where $\phi(\theta)$ is an appropriate hydrogen degradation function; G_{f0} and f_{t0} represent the fracture energy and failure strength at null hydrogen $\theta = 0$. As can be seen, Irwin's internal length $l_{ch} := E_0 G_f / f_t^2$ is not affected by the hydrogen coverage.

Remark 2.1. In the literature, the AT2 model has been adopted in Martínez-Pañeda et al. [38] for the modeling of HAC. The resulting homogeneous solution of the stress – strain relation for a softened bar under uniaxial traction is shown in Fig. 2(a). □

2.1.2. Phase-field regularized cohesive zone model (PF-CZM)

As extensively discussed in Mandal et al. [33], Kumar et al. [28], the above phase-field models for brittle fracture cannot well capture crack nucleation since the length scale parameter b given from Eq. (2.7) might be either too large or too small. This issue was successfully addressed by the phase-field regularized cohesive zone model (PF-CZM) for both brittle and quasi-brittle fracture [64,68].

In the PF-CZM, the crack geometric function is postulated as

$$\alpha(d) = 2d - d^2 \quad \Rightarrow \quad c_\alpha = \pi \quad (2.9)$$

though other parameter $\xi \in (0, 2]$ can also be employed [63]. Moreover, the parameter $a_1 > 0$ in the degradation function (2.3)₂ is not fixed but inversely proportional to the length scale parameter, i.e.,

$$a_1 = \frac{4}{\pi b} l_{ch} \quad (2.10)$$

Compared to the AT1/2 and WN models for brittle fracture, in the PF-CZM the failure strength f_t is an independent material property. The above characteristic functions then result in a particular PF-CZM with linear softening curve [63,64,68].

As the failure strength and fracture energy are independent material parameters, they can be affected by various degradation functions, making the PF-CZM more flexible in the modeling of HAC. For instance, regarding the HEDE mechanism the following two cases can be considered as in Wu et al. [72]

$$\begin{cases} \text{PF-CZM1: } f_t = \phi(\theta)f_{t0}, & G_f(\theta) = \phi(\theta)G_{f0} \quad \Rightarrow \quad l_{ch} = \frac{1}{\phi(\theta)}l_{ch0} \\ \text{PF-CZM2: } f_t = \sqrt{\phi(\theta)}f_{t0}, & G_f(\theta) = \phi(\theta)G_{f0} \quad \Rightarrow \quad l_{ch} = l_{ch0} \end{cases} \quad (2.11)$$

The resulting softening curves are shown in Fig. 2(b) and (c) for various hydrogen coverage.

As can be seen, in the PF-CZM1 the ultimate crack opening displacement w_c keeps constant with respect to the hydrogen coverage θ . That is, Irwin's internal length l_{ch} increases in the presence of hydrogen concentration, resulting in a larger cohesive zone. This HEDE mechanism is in agreement with the theoretical finding of Lee and Unger [30] and has been adopted in the CZM based approach for HAC [58,55,1,15]. Note that in the PF-CZM1, the mechanical degradation function $\omega(d)$ depends on both the damage field $d(x)$ and the hydrogen concentration field $C(x)$ (via the coverage θ).

Comparatively, for the PF-CZM2 both the failure strength f_t and the ultimate crack opening w_c reduce with an increasing hydrogen coverage in such a way that Irwin's internal length l_{ch} is fixed as those phase-field models for brittle fracture [38]. According to Raykar et al. [52] such an HEDE is in line with the observed drop in both ultimate strength and percentage elongation of AS-4340 grade.

Remark 2.2. In the PF-CZM, though the incorporated length scale b can also be regarded as a material property dependent neither on the

failure strength nor on the fracture energy, in this work it is a numerical parameter that can be taken as small as possible. In this context, the Γ -convergence [13] to the CZM is guaranteed for a vanishing length scale $b \rightarrow 0$. Practically, so long as b is sufficiently small compared to the structural characteristic sizes, the numerical prediction is independent of it. In this case, the length scale parameter needs not to be calibrated or adjusted as in the AT1/2 and WN models for brittle fracture. □

2.2. Hydrogen assisted degradation function

Though there exist several hydrogen degradation functions [58,55,1], the following linear one is adopted for the sake of simplicity [38]

$$\phi(\theta) = 1 - \chi\theta \quad (2.12)$$

where the coefficient χ can be estimated by fitting DFT data from the literature. The hydrogen-dependent softening curves shown in Fig. 2 are obtained from the above degradation function (2.12) with the parameter $\chi = 0.89$.

To couple the diffusion problem with the phase-field models for fracture, one needs to connect the surface concentration θ with the bulk one C . According to Serebrinsky et al. [58], this relation is provided by the Langmuir – McLean isotherm [23]

$$\theta = \frac{C}{C + \exp\left(-\frac{\Delta g_b^0}{RT}\right)} \quad (2.13)$$

where C is given in units of impurity mole fraction; Δg_b^0 denotes the Gibbs free energy difference between the adsorbed and bulk standard states. When the bulk concentration C is low, it is more conveniently expressed in the unit of wt. ppm (part per million weight), with C replaced by $5.5 \times 10^{-5}C$ in Eq. (2.13), where the coefficient comes from the unit conversion from wt. ppm to mole fraction.

3. Finite element implementation

In accordance with the weighted residual method, the governing equations and natural boundary conditions in Box 1 can be rewritten as the following weak form: Find $u \in \mathcal{U}$, $C \in \tilde{\mathcal{U}}$ and $d \in \bar{\mathcal{U}}$ such that

$$\begin{cases} \int_{\Omega} \sigma : \nabla^{\text{sym}} \delta u \, dV = \int_{\Omega} \mathbf{b}^* \cdot \delta u \, dV + \int_{\partial \Omega_t} \mathbf{t}^* \cdot \delta u \, dA & \forall \delta u \in \mathcal{V} \\ \int_{\Omega} \dot{C} \, dV & \delta C \, dV \\ - \int_{\Omega} \mathbf{J} \cdot \nabla (\delta C) \, dV & \\ = - \int_{\partial \Omega_f} J^* \delta C \, dA & \forall \delta C \in \tilde{\mathcal{V}} \int_B (\mathbf{q} \cdot \nabla \delta d - Q \delta d) \, dV \geq 0 \quad \forall \delta d \in \bar{\mathcal{V}} \end{cases} \quad (3.1)$$

where we have introduced the following test and trial spaces

$$\begin{cases} \mathcal{U} := \{u | u(\mathbf{x}) = \mathbf{u}^* \, \forall \mathbf{x} \in \partial \Omega_u\}, & \mathcal{V} := \{\delta u | \delta u(\mathbf{x}) = \mathbf{0} \, \forall \mathbf{x} \in \partial \Omega_u\} \\ \tilde{\mathcal{U}} := \{C | C(\mathbf{x}) = C^* \, \forall \mathbf{x} \in \partial \Omega_C\}, & \tilde{\mathcal{V}} := \{\delta C | \delta C(\mathbf{x}) = 0 \, \forall \mathbf{x} \in \partial \Omega_C\} \\ \bar{\mathcal{U}} := \{d | d(\mathbf{x}) \in [0, 1], \dot{d}(\mathbf{x}) \geq 0 \, \forall \mathbf{x} \in B\}, & \bar{\mathcal{V}} := \{\delta d | \delta d(\mathbf{x}) \geq 0 \, \forall \mathbf{x} \in B\} \end{cases} \quad (3.2)$$

The above weak form is ready for a spatial discretization using multi-field finite elements. That is, nodal unknowns are composed by degrees of freedom (dofs) of the displacement, hydrogen concentration and damage. The numerical implementation will be addressed in this section.

3.1. Finite element discretization

In the spatial discretization, the computational domain Ω is triangulated by a mesh \mathcal{T}^h . The super-index h indicates a typical mesh size based on the finite element domain \mathcal{T}^h . It is necessary for the element size h within the localization band \mathcal{B}^h be much smaller than the length scale parameter b , usually $h \leq \frac{1}{5}b$, such that an accurate estimation of the fracture energy can be guaranteed in the discrete context [12].

Upon the above setting, the primary field variables are approximated as

$$\mathbf{u}^h(\mathbf{x}) = \sum_A N_A(\mathbf{x}) \mathbf{a}_A = \mathbf{N} \mathbf{a} \quad (3.3a)$$

$$C^h(\mathbf{x}) = \sum_A \tilde{N}_A(\mathbf{x}) \tilde{a}_A = \tilde{\mathbf{N}} \tilde{\mathbf{a}} \quad (3.3b)$$

$$d^h(\mathbf{x}) = \sum_A \bar{N}_A(\mathbf{x}) \bar{a}_A = \bar{\mathbf{N}} \bar{\mathbf{a}} \quad (3.3c)$$

where $N_A(\mathbf{x})$, $\tilde{N}_A(\mathbf{x})$, and $\bar{N}_A(\mathbf{x})$ are the interpolation functions for the displacement, concentration and damage fields, respectively; \mathbf{N} , $\tilde{\mathbf{N}}$ and $\bar{\mathbf{N}}$ are the corresponding matrix forms. The nodal displacements \mathbf{a}_A , concentrations \tilde{a}_A and damage \bar{a}_A are collectively grouped in vectors \mathbf{a} , $\tilde{\mathbf{a}}$ and $\bar{\mathbf{a}}$, respectively.

The strain field as well as the derivatives of the concentration and damage fields are thus given by

$$\epsilon^h(\mathbf{x}) = \sum_A \mathbf{B}_A(\mathbf{x}) \mathbf{a}_A = \mathbf{B} \mathbf{a} \quad (3.4a)$$

$$\nabla C^h(\mathbf{x}) = \sum_A \tilde{\mathbf{B}}_A(\mathbf{x}) \tilde{a}_A = \tilde{\mathbf{B}} \tilde{\mathbf{a}} \quad (3.4b)$$

$$\nabla d^h(\mathbf{x}) = \sum_A \bar{\mathbf{B}}_A(\mathbf{x}) \bar{a}_A = \bar{\mathbf{B}} \bar{\mathbf{a}} \quad (3.4c)$$

with the compatibility matrices $\tilde{\mathbf{B}}_A$, \mathbf{B}_A and $\bar{\mathbf{B}}_A$ for the strain field $\epsilon(\mathbf{x})$, the concentration gradient field $\nabla C(\mathbf{x})$ and the damage gradient $\nabla d(\mathbf{x})$, respectively.

With the above finite element discretization, the weak form (3.1) yields the following semi-discrete equations

$$\mathbf{R} := \mathbf{f}^{\text{ext}} - \int_{\Omega} \mathbf{B}^T \boldsymbol{\sigma} dV = \mathbf{0} \quad (3.5a)$$

$$\tilde{\mathbf{R}} := \tilde{\mathbf{f}}^{\text{ext}} + \int_{\Omega} \tilde{\mathbf{B}}^T \mathbf{J} dV - \mathbf{C} \tilde{\mathbf{a}} = \mathbf{0} \quad (3.5b)$$

$$\bar{\mathbf{R}} := \int_{\mathcal{B}} \bar{\mathbf{N}}^T Q dV - \int_{\mathcal{B}} \bar{\mathbf{B}}^T \mathbf{q} dV \leq \mathbf{0} \quad (3.5c)$$

where \mathbf{R} , $\tilde{\mathbf{R}}$, and $\bar{\mathbf{R}}$ denote the corresponding residual vectors with respect to the external forces

$$\mathbf{f}^{\text{ext}} = \int_{\Omega} \mathbf{N}^T \mathbf{b}^* dV + \int_{\partial\Omega_t} \mathbf{N}^T \mathbf{t}^* dA \quad (3.6)$$

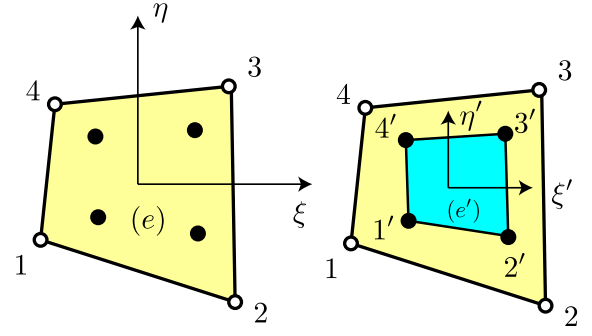


Fig. 3. Four-node quadrilateral bilinear element Q4 and the quadrature points.

$$\tilde{\mathbf{f}}^{\text{ext}} = - \int_{\partial\Omega_f} \tilde{\mathbf{N}}^T J^* dA \quad (3.7)$$

as well as the concentration capacity matrix $\mathbf{C} := \int_{\Omega} \tilde{\mathbf{N}}^T \tilde{\mathbf{N}} dV$ and the nodal concentration rate $\dot{\tilde{\mathbf{a}}} = d\tilde{\mathbf{a}}/dt$.

The system of nonlinear Eqs. (3.5) is usually solved by an incremental-iterative scheme. To this end, the time interval $[0, T]$ of interest are temporally discretized. For a typical time increment $[t_n, t_{n+1}]$ of length $\Delta t := t_{n+1} - t_n$, all state variables are known at the instance t_n . Accordingly, the nodal concentration rate $\dot{\tilde{\mathbf{a}}}$ is approximated using an implicit backward Euler scheme, leading to

$$\tilde{\mathbf{R}} := \Delta t \tilde{\mathbf{f}}^{\text{ext}} + \mathbf{C} \tilde{\mathbf{a}}_n - \left(- \Delta t \int_{\Omega} \tilde{\mathbf{B}}^T \mathbf{J} dV + \mathbf{C} \tilde{\mathbf{a}} \right) = \mathbf{0} \quad (3.8)$$

where Δt denotes the time step and we have omitted the subscript $n+1$ at current instant t_{n+1} .

Remark 3.1. The test and trial spaces introduced in Eq. (3.2)₃ operate on the scalar field variable $d(\mathbf{x})$ that satisfies the damage boundedness condition $d(\mathbf{x}) \in [0, 1]$ and the irreversibility condition $\dot{d}(\mathbf{x}) \geq 0$. In the finite element implementation, the standard test and trial spaces with no constraints are constructed first as those for the concentration field. Regarding the piece-wise linear interpolation functions $\bar{N}_A(\mathbf{x}) \in [0, 1]$, both conditions transform into the following lower and upper bounds [4,65] acting on the nodal phase-field variables \bar{a}_A

$$0 \leq \bar{a}_{A,n} \leq \bar{a}_{A,n+1} \leq 1, \quad \forall A = 1, 2, \dots \quad (3.9)$$

Computationally, the above condition can be dealt with by an optimization solver with lower (updated after the solution converges for a specific iteration) and upper bounds. That is, the residuals (3.5a), (3.8) and (3.5c) are numerically solved upon the bound constraint (3.9); see Section 3.3 for the details. \square

3.2. Gradient of the hydrostatic stress

In Eq. (3.8), the hydrogen flux \mathbf{J} is given by the constitutive relation

$$\mathbf{J} := - \frac{DC}{RT} \nabla \mu = - D \nabla C + \frac{DV_H}{RT} C \nabla \sigma_H \quad (3.10)$$

As can be seen, we need to calculate the gradient $\nabla \sigma_H$ of the hydrostatic stress.

In this work, the hydrostatic stress σ_H is approximated using the same interpolation functions $\bar{N}_A(\mathbf{x})$ as the damage field, i.e.,

$$\sigma_H(\mathbf{x}) = \sum_A \bar{N}_A(\mathbf{x}) \sigma_{H,A} = \bar{\mathbf{N}} \boldsymbol{\Sigma} \quad \Rightarrow \quad \sigma_H(\mathbf{x}_I) = \bar{\mathbf{N}}(\mathbf{x}_I) \boldsymbol{\Sigma} \quad (3.11)$$

where the vector $\boldsymbol{\Sigma}$ collects the nodal hydrostatic stresses $\sigma_{H,A}$ of a specific element, say 'e' in Fig. 3, given by

$$\Sigma = [\bar{\mathbf{N}}(\mathbf{x}_I)]^{-1} \sigma_H(\mathbf{x}_I) \quad (3.12)$$

for the vector $\sigma_H(\mathbf{x}_I)$ collecting the hydrostatic stresses available at all the quadrature points \mathbf{x}_I . Accordingly, in the element 'e' the gradient $\nabla \sigma_H$ of the hydrostress is determined as

$$\nabla \sigma_H = \sum_A \bar{\mathbf{B}}_A(\mathbf{x}) \sigma_{H,A} = \bar{\mathbf{B}} \Sigma = \bar{\mathbf{B}} [\bar{\mathbf{N}}(\mathbf{x}_I)]^{-1} \sigma_H(\mathbf{x}_I) \quad (3.13)$$

As expected, it depends on the interpolation scheme for the hydrostatic stress.

For the sake of simplicity, we consider only 2D problems and a combined Q8/4 element is used in the numerical implementation. More specifically, the quadratic Q8 element (eight-node quadrilateral elements) with four Gaussian quadrature points (reduced integration) is used for the displacement-hydrogen sub-problem (see Section 3.3 for a discussion on the solver), while the damage field is approximated by the Q4 element (consisting of the same corner nodes) with the same four Gaussian quadrature points. Accordingly, it follows that

for every successive time step $n + 1$ do

Initialization: $(\mathbf{a}_{n+1}^{(0)}, \tilde{\mathbf{a}}_{n+1}^{(0)}, \bar{\mathbf{a}}_{n+1}^{(0)}) = (\mathbf{a}_n, \tilde{\mathbf{a}}_n, \bar{\mathbf{a}}_n)$, $k = 1$

while not converged do

 Compute nodal displacements and concentrations $(\mathbf{a}_{n+1}^{(k)}, \tilde{\mathbf{a}}_{n+1}^{(k)})$ with fixed damage field $\bar{\mathbf{a}}_{n+1}^{(k-1)}$

$$\mathbf{R} := \mathbf{f}_{n+1}^{\text{ext}} - \int_{\Omega} \mathbf{B}^T \boldsymbol{\sigma} \, dV = \mathbf{0}, \quad \boldsymbol{\sigma} = \boldsymbol{\sigma}(\mathbf{a}_{n+1}^{(k)}, \tilde{\mathbf{a}}_{n+1}^{(k)}; \bar{\mathbf{a}}_{n+1}^{(k-1)})$$

$$\tilde{\mathbf{R}} := \Delta t \tilde{\mathbf{f}}_{n+1}^{\text{ext}} + \mathbf{C} \tilde{\mathbf{a}}_n - \left(-\Delta t \int_{\Omega} \tilde{\mathbf{B}}^T \mathbf{J} \, dV + \mathbf{C} \tilde{\mathbf{a}}_{n+1}^{(k)} \right) = \mathbf{0}, \quad \mathbf{J} = \mathbf{J}(\mathbf{a}_{n+1}^{(k)}; \tilde{\mathbf{a}}_{n+1}^{(k)})$$

 Compute phase-field dofs $\bar{\mathbf{a}}_{n+1}^{(k)}$ with fixed displacements and concentrations $(\mathbf{a}_{n+1}^{(k)}, \tilde{\mathbf{a}}_{n+1}^{(k)})$

$$\bar{\mathbf{R}} := - \int_{\mathcal{B}} \left[\bar{\mathbf{N}}^T \left(\omega' \bar{\mathbf{Y}} + \frac{1}{c_\alpha b} \alpha' G_f \right) + \frac{2b}{c_\alpha} G_f \bar{\mathbf{B}}^T \nabla d \right] dV \leq \mathbf{0}$$

 subjected to: $0 \leq \bar{a}_{In} \leq \bar{a}_{In+1}^{(k)} \leq 1 \quad \forall I = 1, 2, \dots$

$$\omega' := \omega'(\bar{\mathbf{a}}_{n+1}^{(k)}, \tilde{\mathbf{a}}_{n+1}^{(k)}), \quad \alpha' := \alpha'(\bar{\mathbf{a}}_{n+1}^{(k)}), \quad \bar{\mathbf{Y}} := \bar{\mathbf{Y}}(\mathbf{a}_{n+1}^{(k)})$$

 Set $k = k + 1$

Update nodal unknowns: $(\mathbf{a}_{n+1}, \tilde{\mathbf{a}}_{n+1}, \bar{\mathbf{a}}_{n+1}) = (\mathbf{a}_{n+1}^{(k)}, \tilde{\mathbf{a}}_{n+1}^{(k)}, \bar{\mathbf{a}}_{n+1}^{(k)})$

$$[\bar{\mathbf{N}}(\xi, \eta)]^{-1} = \begin{bmatrix} 1 + \frac{\sqrt{3}}{2} & -\frac{1}{2} & 1 - \frac{\sqrt{3}}{2} & -\frac{1}{2} \\ -\frac{1}{2} & 1 + \frac{\sqrt{3}}{2} & -\frac{1}{2} & 1 - \frac{\sqrt{3}}{2} \\ 1 - \frac{\sqrt{3}}{2} & -\frac{1}{2} & 1 + \frac{\sqrt{3}}{2} & -\frac{1}{2} \\ -\frac{1}{2} & 1 - \frac{\sqrt{3}}{2} & -\frac{1}{2} & 1 + \frac{\sqrt{3}}{2} \end{bmatrix} \quad (3.14)$$

corresponding to the four quadrature points 1', 2', 3' and 4'; see Fig. 3 for the illustration. Extension to high order elements such as is straightforward. The use of Q4 elements for the damage field not only reduces the cost but also it might enable us to use completely different meshes for the damage sub-problem and the displacement/hydrogen sub-problem.

3.3. Alternating minimization solver

As the underlying energy functional to be minimized is non-convex [11,12], the Newton method based monolithic algorithm is not robust enough in solving the residuals (3.5a), (3.8) and (3.5c). To circumvent this issue, either the BFGS quasi-Newton algorithm or the alternate minimization (AM) one can be employed to solve the nodal unknowns $(\mathbf{a}, \tilde{\mathbf{a}}, \bar{\mathbf{a}})$; see Wu and Huang [66], Wu et al. [71] for the case of purely mechanical problems, also Mandal et al. [36] for thermo-mechanical problems.

In this work the AM solver summarized in Algorithm 1 is adopted due to its simplicity. More specifically, the nodal displacements and hydrogen concentrations $(\mathbf{a}, \tilde{\mathbf{a}})$ are first solved from Eqs. (3.5a) and (3.8) with the crack phase-field $\bar{\mathbf{a}}$ fixed, in a monolithic manner using standard Newton-Raphson algorithm. With the updated unknowns $(\mathbf{a}, \tilde{\mathbf{a}})$, the phase-field Eq. (3.5c) with the boundedness condition (3.9) is then solved using the 'Reduced Space Method' as described in Benson and Munson [9].¹ The AM iteration continues until a specific stop criterion,

e.g., the phase-field difference $|\bar{\mathbf{a}}_{n+1}^{(k+1)} - \bar{\mathbf{a}}_{n+1}^{(k)}| < \epsilon$ between two consecutive AM iterations for a small positive number $\epsilon = 1.0 \times 10^{-5}$, is reached.

Algorithm 1. AM smechnical-hydrogen-damageproblem.

Remark 3.2. In phase-field models for fracture, the so-called one-pass staggered solver suggested in Miehe et al. [42] has been widely adopted. Compared to the above multi-pass AM algorithm, no iteration is considered between the damage sub-problem and the mechanical (-diffusion) one. That is, they are decoupled. This one-pass staggered solver was also adopted in the context of hydrogen assisting cracking

¹ From a user point of view, except that the active set of equations subjected to the bound constraint has to be determined in an iterative manner, it is not much different from the standard Newton-Raphson method.

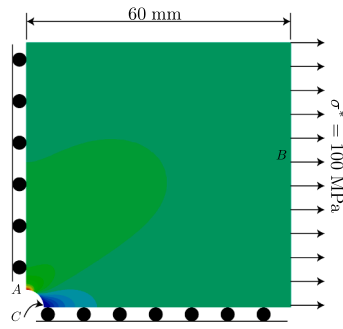


Fig. 4. Elastic plate with a hole: Geometry of a quater, boundary and loading conditions. The hole has a radius of 4 mm.

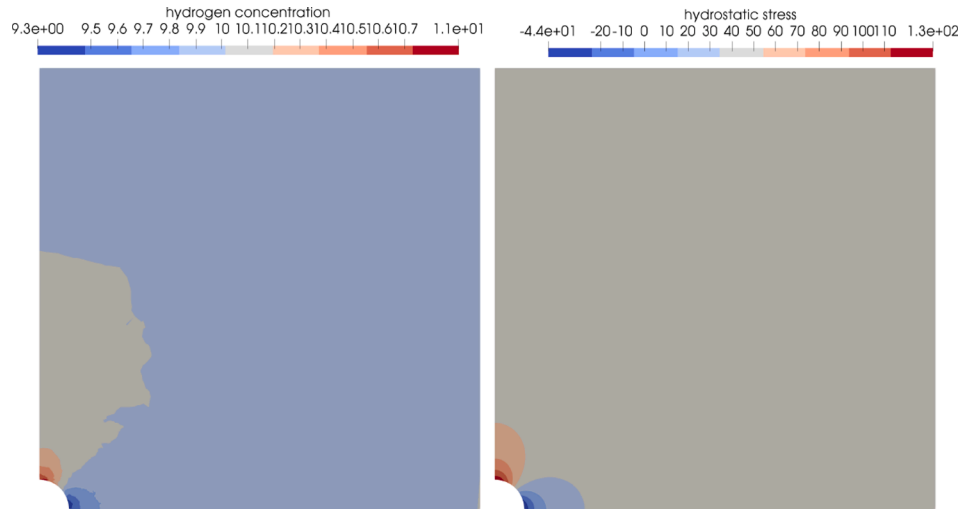


Fig. 5. Elastic plate with a hole: distribution of the concentration (left) and the hydrostatic stress (right) at $t = 3.0 \times 10^4$ s.

[38]. As stated in Ambati et al. [2] for purely mechanical problems, the one-pass staggered algorithm yields acceptable numerical results provided that sufficiently small increments (usually less than 10^{-5}) or adaptive time stepping strategies [26] are used. However, when the post-peak behavior is of interest, this decoupled algorithm should be cautiously used. We confirm this finding in Section 4.2.1 in the presence

of hydrogen. \square

4. Numerical examples

With the numerical implementation presented in Section 3, the phase-field damage models presented in Section 2 are implemented in

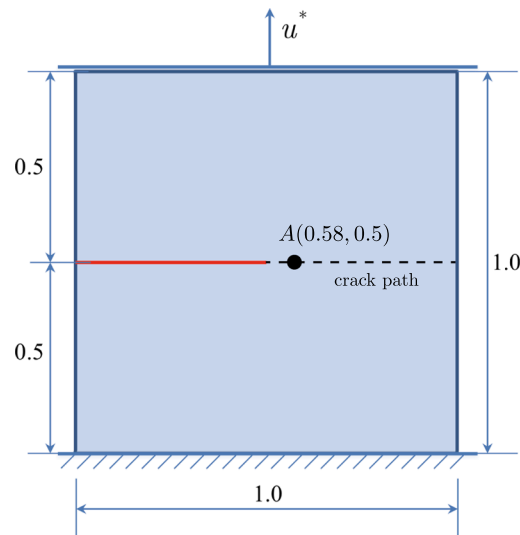


Fig. 6. Single-edge notched plate: Geometry (unit of length: mm), boundary and loading conditions.

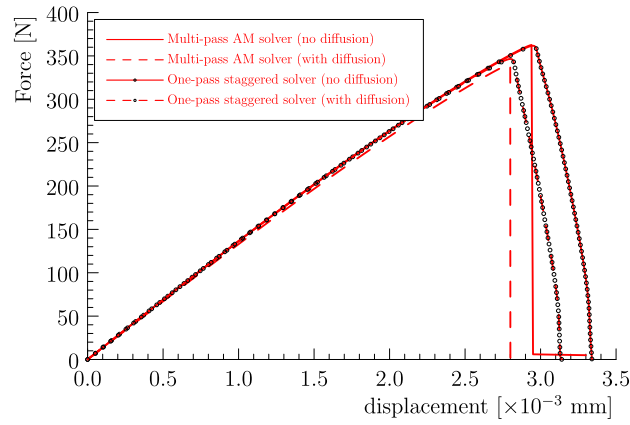


Fig. 7. Single-edge notched plate: the AT2 model solved by the one-pass and multi-pass AM solvers.

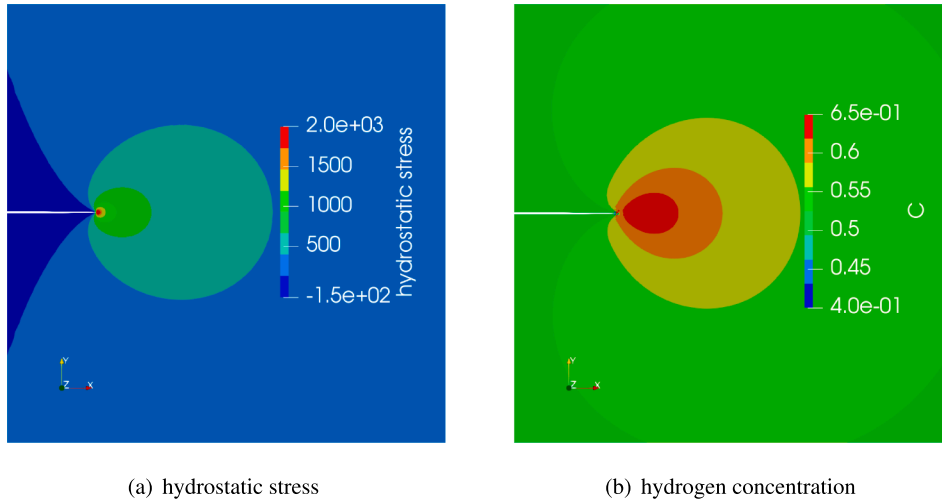


Fig. 8. Single-edge notched plate: hydrostatic stress and hydrogen concentration near peak load predicted by the AT2 model.

feFRAC — our in-house FE code based on the open-source library jive [48]. Finite element meshes are generated using Gmsh [20] and visualization is performed in Paraview [6].

Using the FE code feFRAC, we address in this section a set of numerical examples to demonstrate the performances of the AT2 model, the PF-CZM1 and PF-CZCM2 for HAC. Unless otherwise explicitly

specified, material parameters related to the hydrogen diffusion equation are [58,38]: $T = 300$ K, $\Delta g_b^0 = 30$ kJ/mol, $R = 8.314$ J/(mol K) and $V_H = 2000$ mm³/mol. Iron-based materials are considered in these examples. Consequently, the elastic constants are adopted as Young's modulus $E_0 = 2.1 \times 10^5$ MPa, Poisson's ratio $\nu_0 = 0.3$, and a hydrogen degradation coefficient of $\chi = 0.89$ is assumed in Eq. (2.12).

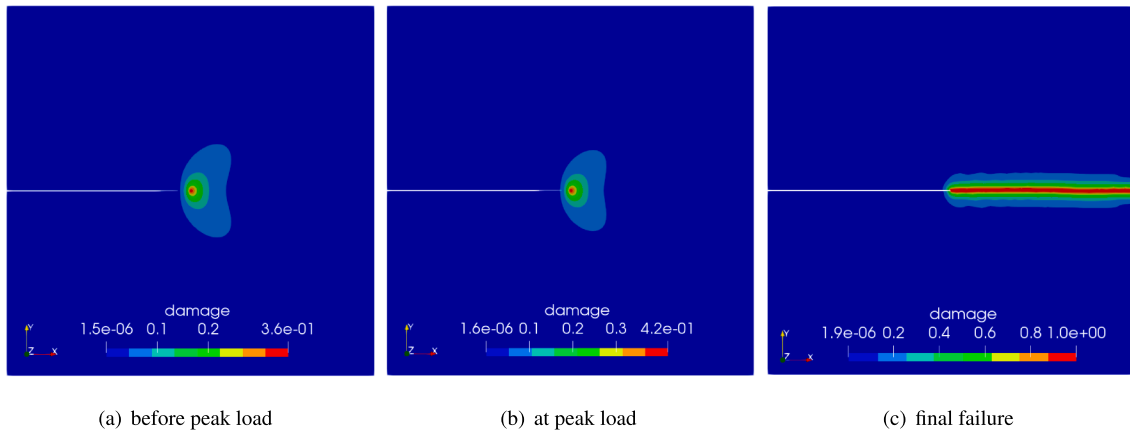


Fig. 9. Single-edge notched plate: crack propagation process predicted by the AT2 model.

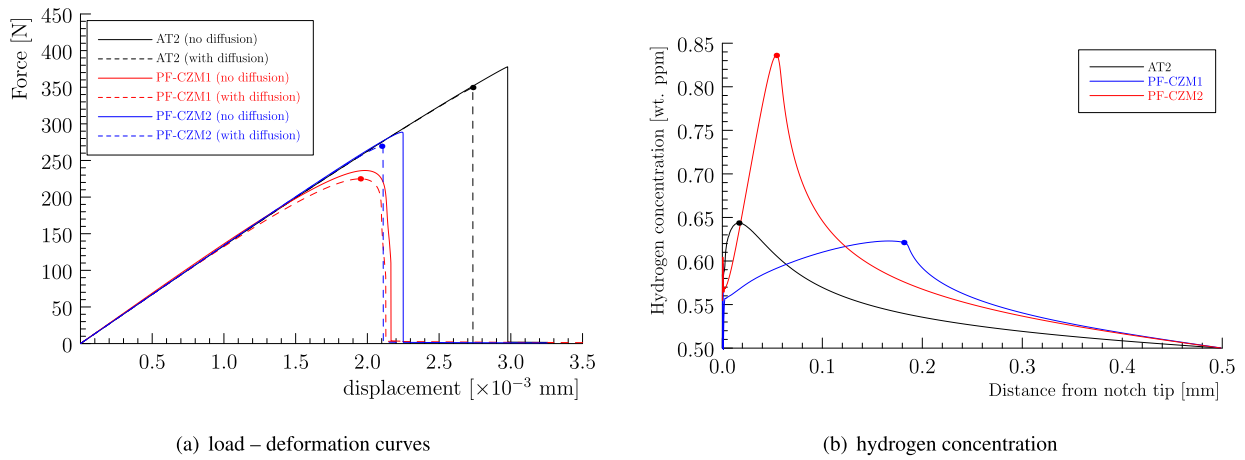


Fig. 10. Single-edge notched plate: Effect of hydrogen concentration.

Remark 4.1. In order to study the effect of the length scale parameter, only the early versions [11,12,42] of the AT2 model is considered in this work. In such a model, the length scale parameter is a numerical parameter such that the Γ -convergence is guaranteed. Consequently, the

relevant results presented in this section do not apply to the later versions [49,61] of the AT1/2 models in which the length scale is treated as a material property determined by Eq. (2.7). \square

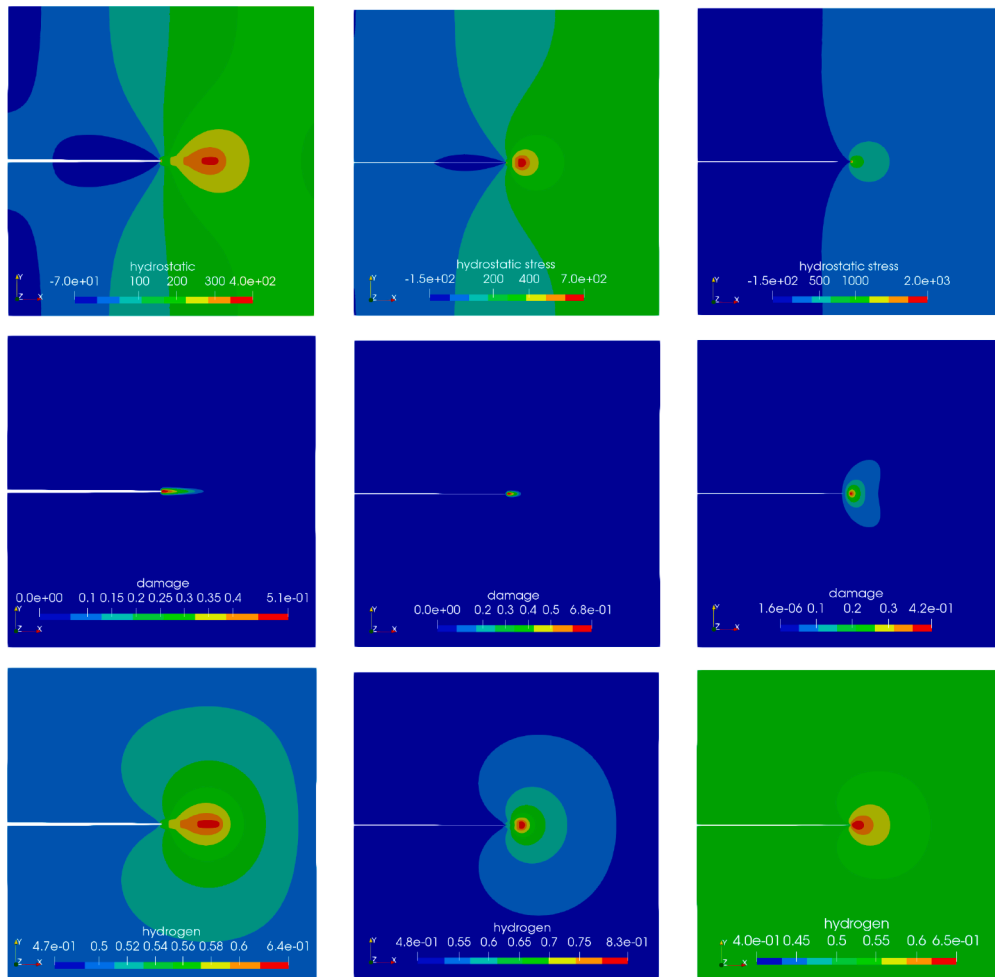


Fig. 11. Single-edge notched plate: Distributions of the hydrogen concentration, crack phase-field and hydrostatic stress at the peak load for various models (left column: AT2; middle column: PF-CZM1; right column: PF-CZM2).

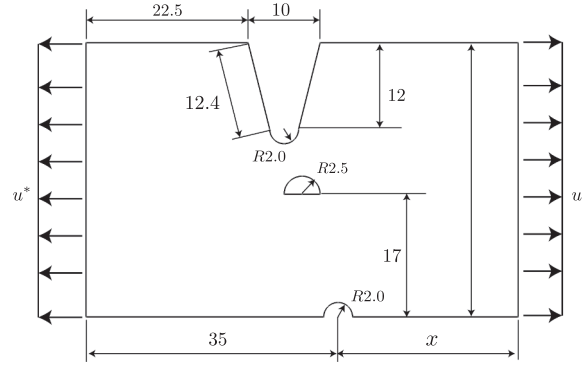


Fig. 12. Plate with existing defects: geometry and loading. Dimensions are given in mm.

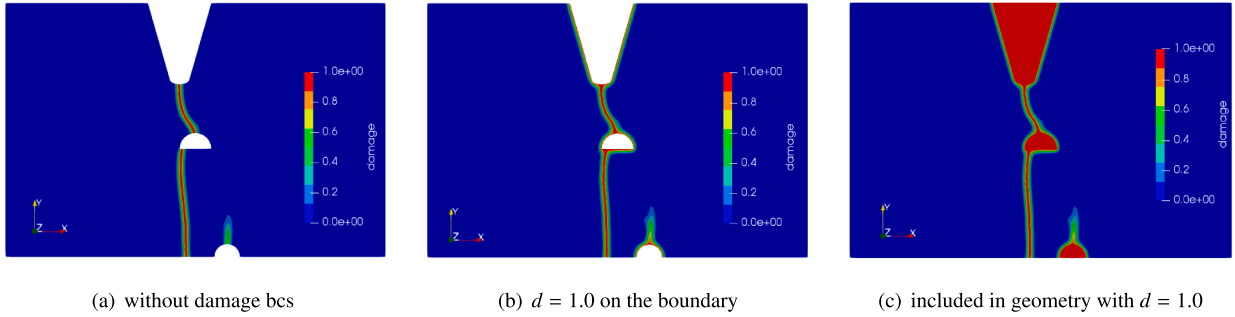


Fig. 13. Corrosion pits problem: damage patterns obtained from the three modeling strategies for the pits ($x = x_1 = 25$ mm).

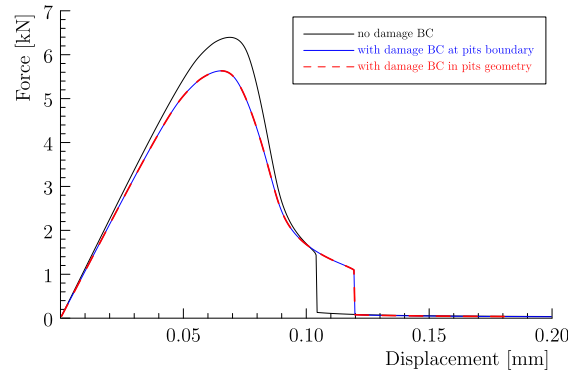


Fig. 14. Corrosion pits problem: load – displacement curves obtained from the three modeling strategies for the pits ($x = x_1 = 25$ mm).

4.1. Elastic plate with a hole

As shown in Fig. 4, a quarter of a square plate with a hole is considered [8]. The right edge is subjected to a uniform stress $\sigma^* = 100$ MPa. All boundaries are insulated so that there is no hydrogen flux away from the plate. An initial uniform distribution of the concentration $C_0 = C_b = 10$ wt ppm is assumed.

Plane strain condition is assumed. The bulk diffusivity is $D = 3.8 \times 10^{-2}$ mm²/s. The simulation time is chosen sufficiently large ($t = 3 \times 10^4$ s) with a fixed time step $\Delta t = 1.0$ s so that a steady state with a uniform chemical potential can be achieved. By choosing two points with known hydrostatic stresses, it is possible to determine the concentration of one point with the value at the other point known.

Due to stress concentration around the hole, the stresses σ_{xx} along axis x and the hydrostatic stresses σ_H at points A, B and C are given by

$$\sigma_{xx,A} = 3\sigma^* = 300 \text{ MPa} \quad \Rightarrow \quad \sigma_{H,A} = \frac{1+\nu_0}{3}\sigma_{xx,A} = 130 \text{ MPa} \quad (4.1a)$$

$$\begin{aligned} \sigma_{xx,B} = -\sigma_{xx,C} = \sigma^* = 100 \text{ MPa} \quad \Rightarrow \quad \sigma_{H,B} = -\sigma_{H,C} = \frac{1+\nu_0}{3}\sigma_{xx,B} \\ = 43.3 \text{ MPa} \end{aligned} \quad (4.1b)$$

At the steady state it follows from $\mu_A = \mu_B$ and $\mu_C = \mu_B$ that

$$C_A = C_b \exp\left(V_H \frac{\sigma_{H,A} - \sigma_{H,B}}{RT}\right) = 10.7199 \text{ wt ppm} \quad (4.2a)$$

$$C_C = C_b \exp\left(V_H \frac{\sigma_{H,C} - \sigma_{H,B}}{RT}\right) = 9.3287 \text{ wt ppm} \quad (4.2b)$$

for the hydrogen concentration $C_B = C_b = 10.0$ wt ppm.

With a mesh consisting of 10757 Q8/4 elements and 10674 nodes, the predicted distributions of the concentration and hydrostatic stress are depicted in Fig. 5, both achieving the maximum and minimum values at points A and C, respectively. The numerical solutions for C_A and C_C are 10.9047 wt ppm and 9.2941 wt ppm, respectively, agreeing well with the analytical results. This agreement validates the numerical implementation of the coupled mechanical-diffusion equations and in particular, the calculation of the gradient of the hydrostatic stress.

4.2. Single-edge notched plate

Let us now consider a single-edge notched plate under tension. As shown in Fig. 6, it is a square plate of length 1 mm. A straight horizontal notch of length 0.5 mm is introduced at the mid-height of the left edge. The bottom edge is fixed, while a vertical displacement is applied to the top edge. Being a popular benchmark test verifying phase-field models for brittle fracture [42,2,68], this example is revisited here as in Martínez-Pañeda et al. [38], Wu et al. [72] to incorporate the hydrogen effect.

The material mechanical parameters are taken from Wu and Nguyen [68], i.e., the fracture toughness $G_{f0} = 2.7$ N/mm and the failure strength $f_{f0} = 2445.42$ MPa (corresponding to that for the AT2 model with the length scale parameter $b = 0.015$ mm), resulting in Irwin's characteristic length $l_{ch} = 0.095$ mm. The hydrogen diffusivity is taken as $D = 0.0127$ mm²/s. A constant hydrogen concentration C^* is prescribed to all external boundaries (including the crack faces), and an initial uniform distribution of concentration $C_0(x) = C^*$ is assumed (in the transient analysis). The applied displacement rate is 10^{-9} mm/s for a total time $t = 10^7$ s. In the numerical simulations, we have used a constant displacement increment $\Delta u^* = 10^{-6}$ mm with the time increment $\Delta t = 10^3$ s.

The following two cases are considered in the simulations.

- (i) A steady state (no diffusion) of the uniform concentration $C = 0.5$ wt ppm, and
- (ii) A transient state (with diffusion) of concentration with $C^* = 0.5$ wt ppm

In the simulations, the mesh size is $h = 0.001$ mm (about 148000 Q8/4 elements) within the damage sub-domain encompassing the crack path.

This section is organized as follows. Section 4.2.1 compares the one-pass staggered and multi-pass AM solvers for the AT2 model. Section 4.2.2 presents a comparison of different models (AT2, PF-CZM1 and PF-CZM2) for HAC.

4.2.1. AM solver: Multi-pass vs. one-pass

Let us first discuss the influence of the AM/staggered iterations on the numerical results. The Abaqus code provided in Martínez-Pañeda et al. [38] and our code `feFRAC`, both for the AT2 model with $b = 0.015$ mm, are adopted. Note that the former code corresponds to the one-pass staggered algorithm, while the latter employs the multi-pass AM solver summarized in Algorithm 1.

To evaluate the effects of the solver, we compare the predicted force – displacement curves (Fig. 7). The post peak responses given by both solvers are different. Remarkably, the multiple-pass AM solver yields perfectly brittle responses, while the one-pass staggered algorithm spuriously delays crack propagation, similarly to that discussed in Ambati et al. [2] for purely mechanical problems. Using smaller increments or adaptive time stepping [26] may alleviate this issue but we did not pursue such a strategy here. Therefore, the multi-pass AM solver is used all along hereafter in this work.

Moreover, the peak load of case (i) is higher than that of case (ii), since hydrogen is transported to the crack tip in the latter where larger hydrostatic stresses result in higher hydrogen concentrations; see Fig. 8.

Fig. 9 shows the crack propagation process: similarly to the case with no hydrogen — the crack nucleates at the notch tip and propagates horizontally to the right edge in a brittle manner.

4.2.2. Various models: AT2, PF-CZM1 and PF-CZM2

The AT2 model with $b = 0.015$ mm, the PF-CZM1 and PF-CZM2 both with $b = 0.01$ mm, are then compared. All these models have an identical failure strength $f_t = 2445.42$ MPa. The predicted force – displacement curves are given in Fig. 10(a).

As can be seen, the PF-CZM1 gives the lowest peak load. This result is expected since in this model the tensile strength f_t is affected most by the factor $\phi(\theta)$ due to the presence of hydrogen. Moreover, as shown by solid lines (with diffusion) and dash lines (with no diffusion) on the same figure, in all the three models the load – deformation responses are affected considerably by the hydrogen diffusion. In particular, except the PF-CZM1 model which shows a certain degree quasi-brittle behavior (around the peak load), the other two models predict brittle responses. This is because that in the PF-CZM1 Irwin's internal length l_{ch} increases in the presence of hydrogen concentration, while in the other two it remains fixed.

Fig. 10(b) presents the variation of the hydrogen concentration along the crack path at peak load. Due to the distinct HEDE mechanisms accounted for, it is not surprising that the distribution of the hydrogen concentration for the PF-CZM1 deviates largely from those for the AT2 model and PF-CZM2.

The distributions of the crack phase-field, hydrogen concentration and hydrostatic stress at peak load for various models are shown in Fig. 11. As can be seen, the support of the damage profile given by AT2 is much larger than those by the PF-CZM1 and PF-CZM2, which is consistent with the purely mechanical case. Moreover, the more brittle the material is, the larger variation the hydrogen concentration and hydrostatic stress exhibit.

4.3. Crack growth from corrosion pits

The final example involves a complex crack path due to existing defects (i.e., corrosion pits) which is accelerated by hydrogen embrittlement (Fig. 12). This problem was proposed by Martínez-Pañeda et al. [38] and later considered in Wu et al. [72]. In this work we re-consider this problem, focusing on the comparison of various phase-field models for HAC.

The following material parameters are adopted [38,72]: the fracture energy $G_f = 90$ N/mm, the failure strength $f_t = 1778.78$ MPa (corresponding to that for the AT2 model with the length scale $b = 0.6$ mm). The bulk diffusivity is $D = 1.0 \times 10^{-8}$ mm²/s. A constant concentration C_b is prescribed to all external boundaries, and an initial uniform distribution of concentration $C_0(x) = C_b = 1.0$ wt ppm is assumed. The load is applied via an imposed displacement u^* with an increment 0.04×10^{-2} mm/s.

This section is organized as follows. In Section 4.3.1, three options of modeling corrosion pits are discussed. Effect of the location of the bottom corrosion pit on the damage pattern is studied in Section 4.3.2. Evolution of damage with and without hydrogen concentration is discussed in Section 4.3.3. And finally a study on the length scale sensitivity is provided in Section 4.3.4.

4.3.1. Various modeling strategies of corrosion pits

There are three modeling strategies for pre-existing notches and voids adopted in the phase-field modeling of fracture [25,61]: (a) excluding them from the geometry as in Fig. 13(a), or (b) excluding them from the geometry but imposing appropriate Dirichlet bcs $d = 1.0$ on the boundary as in Fig. 13(b), or (c) including them in the geometry and assigning the damage field $d = 1$ as if there are no material in these regions as in Fig. 13(c). It seems that there is no agreement upon which strategy should be adopted. Consequently, many researchers use

Table 1
Corrosion pits problem: effect of pit location and damage boundary condition on damage pattern for $C = 0.0$

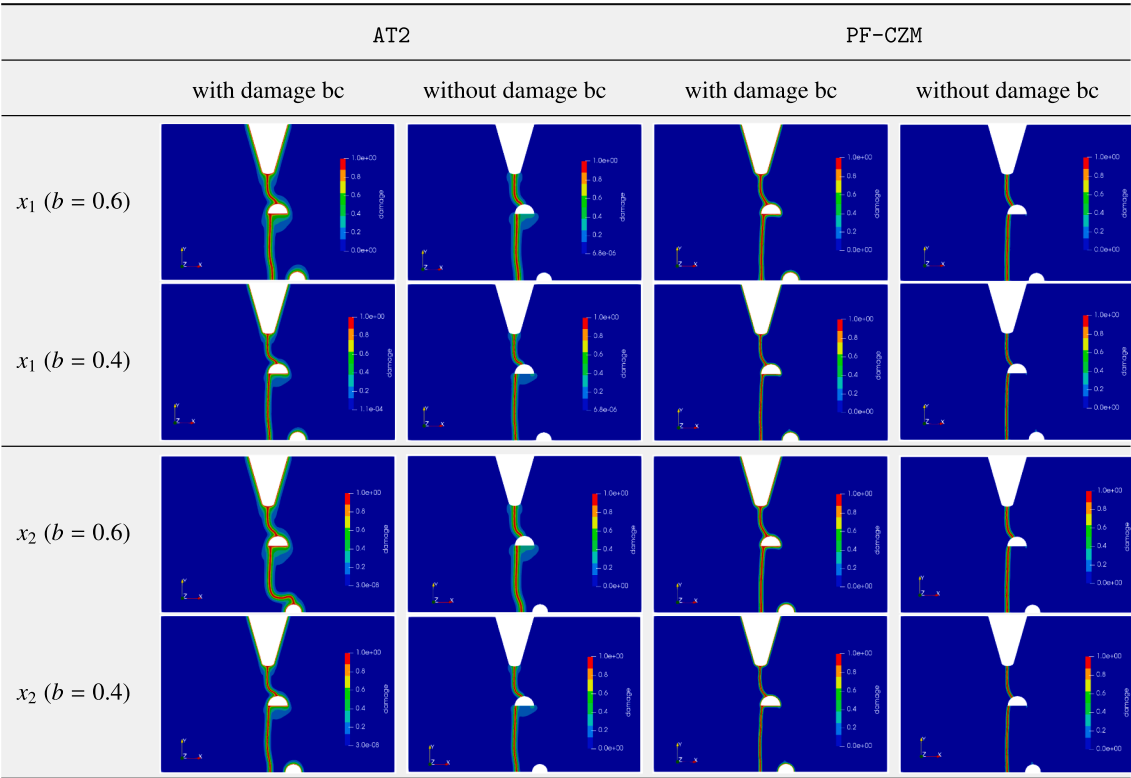


Table 2
Corrosion pits problem: effect of pit location and damage boundary condition on damage pattern for $C = 1.0$

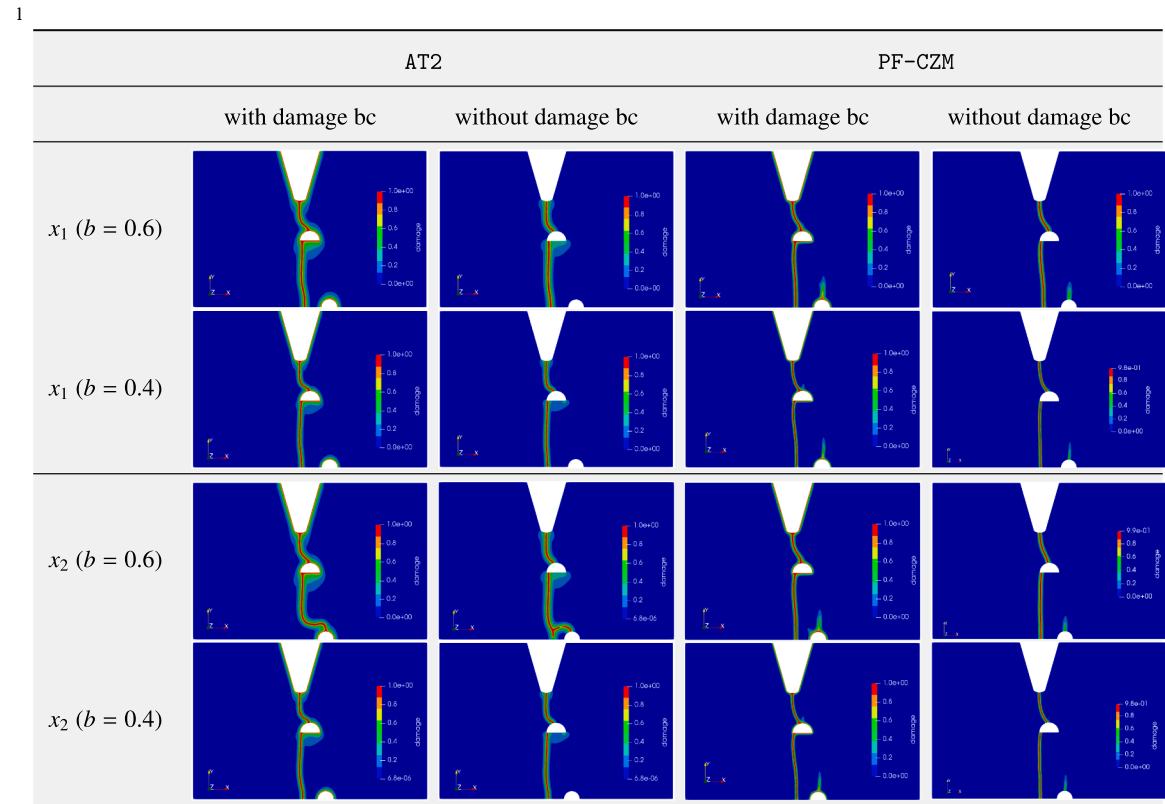
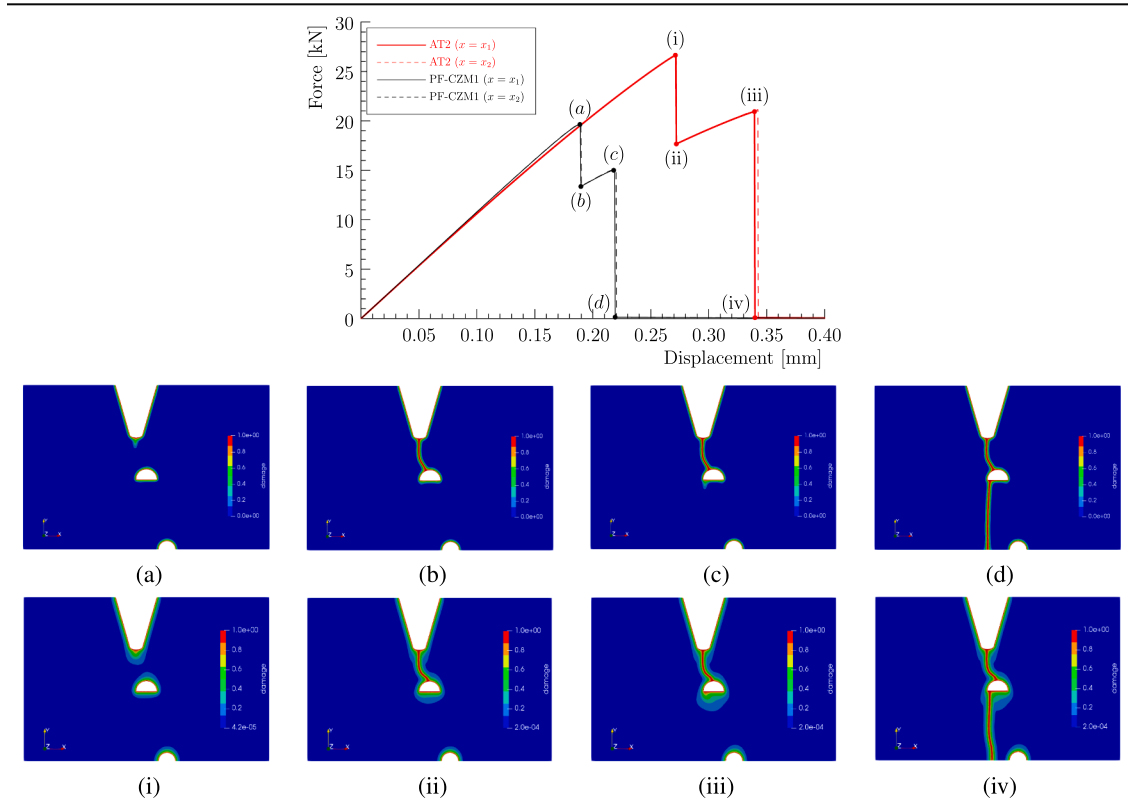


Table 3Corrosion pits problem: load-deformation response (top) and damage evolution (bottom) for $C = 0.0$ 

different options for various problems [70].

Aiming to answer the above question, we consider a uniform hydrogen concentration of 1.0 wt. ppm with no diffusion. The PF-CZM1 is used with the length scale parameter $b = 0.6$ mm. The problem is discretised using 60 000 Q8/4 elements, with the mesh size $h = 0.1$ mm within the damage sub-domain.

As shown in Fig. 13, the damage pattern predicted from these three strategies are almost identical. However, the load – displacement responses presented in Fig. 14 are different: strategy (a) gives the highest peak load, while the other two options yield identical responses. This result is in line with those made by Klinsmann et al. [25], Tanné et al. [61] for purely mechanical problems. This is because that for strategy (a) the energy barrier associated with localization from an undamaged state to a fully softened one needs to be first overcome. In the following, we use strategy (b) unless otherwise specified, since it is less computationally expensive than strategy (c). This is different from that we adopted in Wu et al. [72].

4.3.2. Effect of pit location and damage boundary conditions

As the crack pattern is sensitive to the location of the bottom pit, we further study two locations of that pit, i.e., $x = x_1 = 25$ mm and $x = x_2 = 26$ mm denoted in Fig. 12.

The following modeling strategies are considered: (i) with and without damage boundary conditions at the pits, i.e., strategies (a) and (b), respectively, (ii) two different length scale parameters, i.e., $b = \{0.4, 0.6\}$ mm, (iii) two locations of the bottom corrosion pit $x = x_1 = 25$ mm and $x = x_2 = 26$ mm, and (iv) two phase-field models, i.e., the AT2 model and PF-CZM1.

The numerical results are tabulated in Table 1 for the case with no hydrogen ($C = 0$) and Table 2 for the one with hydrogen ($C = 1.0$ wt ppm). Since the diffusion coefficient for this problem is very small, the effect of hydrogen diffusion is negligible (namely, a uniform hydrogen

concentration and a transient concentration yield identical results) and thus not considered for this study.

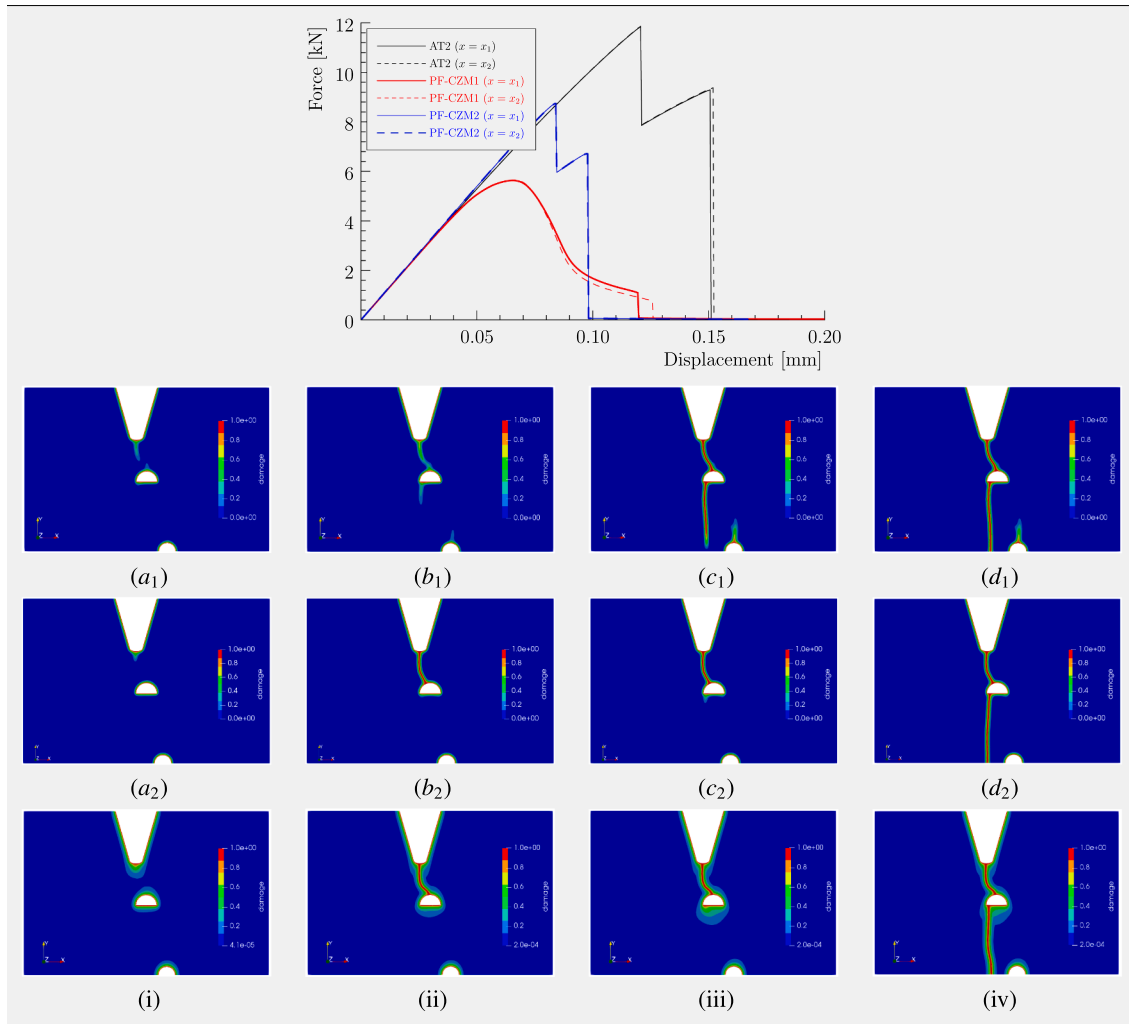
As shown in the right two columns of Tables 1,2, the PF-CZM1 predicts a single crack path from top to bottom without hydrogen. Regarding the case with hydrogen, a similar crack pattern is obtained but with additional crack initiation at the top surface of the bottom pit. That is, for both cases with/without presence of hydrogen the PF-CZM1 gives crack patterns which are insensitive to the length scale, damage boundary condition and the location of the bottom corrosion pit.

A similar damage pattern is observed using the AT2 model for the case without hydrogen. However, it is sensitive to the damage boundary conditions and length scale parameter; see the left two columns of Tables 1,2 for the case of $x = x_2 = 26$ mm and $b = 0.6$ mm.

4.3.3. Damage evolution with/without hydrogen

As shown in Table 3, for the case without hydrogen ($C = 0$) the cracking patterns predicted from both the AT2 model and PF-CZM1 are quite similar. Regarding the latter model, at about $u^* = 0.19$ mm, a first crack nucleates at the top pit and then grows in a brittle manner (resulting in the first drop of the load – displacement curves) towards the second one. At about $u^* = 0.22$ mm a second crack nucleates at the middle pit and propagates vertically to the bottom edge (resulting in the second drop of the load – displacement curve and final failure). For the AT2 model though the crack pattern is similar but the process is quite delayed, resulting in larger peak load.

For the case with hydrogen ($C = 1.0$ wt ppm), the load – displacement behavior and damage evolution predicted by the AT2 model, PF-CZM1 and PF-CZM2 are quite different as shown in Table 4. It can be seen that the PF-CZM1 gives the least peak load and exhibits cohesive fracture behavior whereas the PF-CZM2 shows a typical brittle fracture similarly to the AT2 model. However, the crack patterns given by the three models are similar: a crack nucleates at the top pit and grows a bit,

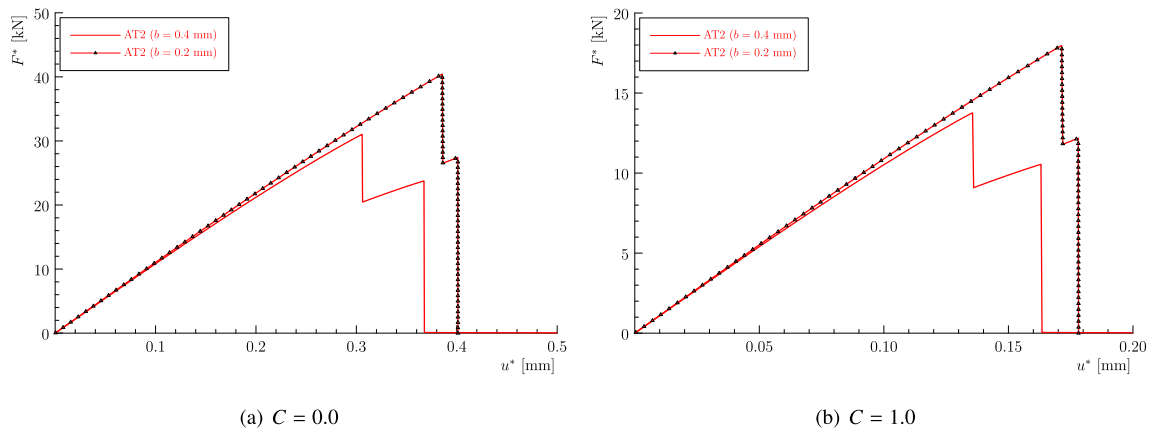
Table 4Corrosion pits problem: load-deformation response (top) and damage evolution (bottom) for $C = 1.0$ wt.ppm

then another crack initiates at the top surface of the middle pit. Subsequently these two cracks merge; then, another crack initiates at the bottom surface of the second pit and propagates downward to the bottom edge of the specimen before the crack nucleating from bottom edge reaches it. Note that the damage bandwidth of the AT2 model is much larger than the PF-CZM1 and PF-CZM2. Large damage zones are prone

to merging together or to be attracted by holes [68,70].

4.3.4. Length scale sensitivity analysis

To study the effect of the length scale parameter, two different values, i.e., $b = 0.4$ mm and $b = 0.2$ mm, are considered. The corresponding mesh sizes within the damage sub-domain are taken as $h =$

**Fig. 15.** Corrosion pits problem: effect of length scale parameter for the AT2 model.

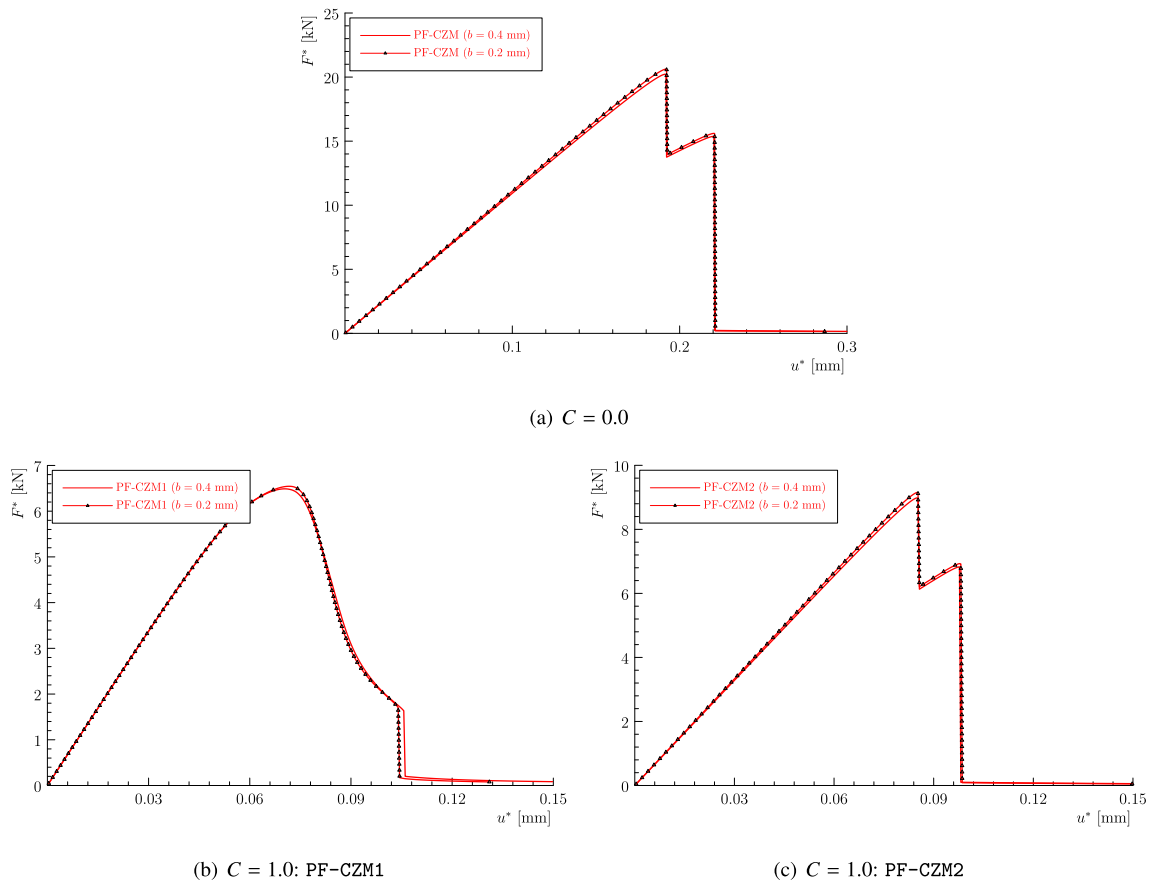


Fig. 16. Corrosion pits problem: effect of length scale parameter for $C = 1.0$ wt. ppm.

$b/5$, i.e., $h = 0.08$ mm (around 70,000 Q8/4 elements) for $b = 0.4$ mm and $h = 0.04$ mm (about 295,000 Q8/4 elements) for $b = 0.2$ mm.

Fig. 15 depicts the load – displacement curves given from the AT2 model for the case with/without hydrogen. As can be seen, the predicted peak loads are sensitive to the length scale parameter.

Comparatively, the global responses predicted by the PF-CZM1 and PF-CZM2 are both independent of the mesh size and the length scale parameter for the cases with/without hydrogen; see Fig. 16. The above results confirm those conclusions drawn from our previous work on purely mechanical problems [63–65,68] and on hydrogen assisted crack [72], though distinct strategies are adopted for the modeling of corrosion pits.

5. Conclusions

In this work we have provided a comparative study of three frequently adopted phase-field models for the hydrogen assisted cracking. Both the phase-field models for brittle fracture (the AT1/2 and WN models) and the phase-field regularized cohesive zone model (PF-CZM) are considered within the unified phase-field theory for damage and fracture, and are extended to incorporate the hydrogen enhanced decohesion (HEDE) mechanism. In the first group, the failure strength is a dependent material property related to the fracture energy and the length scale parameter. Consequently, only the HEDE mechanism, in which the failure strength and fracture energy are degenerated according to a single hydrogen degradation function, can be accounted for. Contrariwise, in the second PF-CZM group, the failure strength is an independent material parameter such that a hydrogen degradation function different from that of the fracture energy can be adopted. Therefore, it is possible to deal with various HEDE mechanisms resulting

in Irwin's characteristic length larger, less than or equal to the initial value with no hydrogen.

The numerical implementation of the phase-field models for hydrogen assisted cracking has also been presented. In particular, a scheme necessary for calculating the gradient of the hydrostatic stress has been presented. Representative numerical examples show that, the one-pass staggered solver should be used with cautions for it largely delays damage evolution. Moreover, for the widely adopted AT2 model the length scale parameter should be carefully treated to avoid sensitive results. Comparatively, the PF-CZM1 with increasing Irwin's characteristic length and the PF-CZM2 with constant Irwin's length are both insensitive to the regularization length scale parameter as their purely mechanical counterpart PF-CZM. This merit makes them appropriate for the modeling of hydrogen assisted cracking, but more research work on rationally modeling the HEDE mechanism and significantly improving the computational efficiency needs to be done in the near future.

Declaration of Competing Interest

The authors declare that they have no known competing financial interests or personal relationships that could have appeared to influence the work reported in this paper.

Acknowledgments

This work is supported by the National Natural Science Foundation of China (51878294; 51678246), the State Key Laboratory of Subtropical Building Science (2018ZC04) to the third author (J.Y. Wu). Tushar Kanti Mandal thanks the Monash Graduate Scholarship and Monash International Tuition Scholarship for funding his PhD. Vinh Phu Nguyen

thanks the funding support from the Australian Research Council via DECRA project DE160100577. The authors would like to express the gratitude towards Dr. Erik Jan Lingens at the Dynaflow Research Group, Houtsingel 95, 2719 EB Zoetermeer, the Netherlands for providing support on the numerical toolkit Jive.

References

- [1] A. Alvaro, I.T. Jensen, N. Kheradmand, O. Løvvik, V. Olden, Hydrogen embrittlement in nickel, visited by first principles modeling, cohesive zone simulation and nanomechanical testing, *Int. J. Hydrogen Energy* 40 (47) (2015) 16892–16900.
- [2] M. Ambati, T. Gerasimov, L. de Lorenzis, A review on phase-field models for brittle fracture and a new fast hybrid formulation, *Comput. Mech.* 55 (2015) 383–405.
- [3] M. Ambati, R. Kruse, L. De Lorenzis, A phase-field model for ductile fracture at finite strains and its experimental verification, *Comput. Mech.* 57 (1) (2016) 149–167.
- [4] H. Amor, J. Marigo, C. Maurini, Regularized formulation of the variational brittle fracture with unilateral contact: numerical experiments, *J. Mech. Phys. Solids* 57 (2009) 1209–1229.
- [5] P. Areias, T. Rabczuk, M.A. Msek, Phase-field analysis of finite-strain plates and shells including element subdivision, *Comput. Methods Appl. Mech. Eng.* 312 (2016) 322–350.
- [6] U. Ayachit, *The ParaView guide: a parallel visualization application*. Kitware, ISBN 978-1930934306, 2015.
- [7] G.I. Barenblatt, The formation of equilibrium cracks during brittle fracture. General ideas and hypotheses. axially-symmetric cracks, *J. Appl. Math. Mech.* 23 (1959) 622–636.
- [8] O. Barrera, E. Tarleton, H. Tang, A. Cocks, Modelling the coupling between hydrogen diffusion and the mechanical behaviour of metals, *Comput. Mater. Sci.* 122 (2016) 219–228.
- [9] S.J. Benson, T.S. Munson, Flexible complementarity solvers for large-scale applications, *Optim. Methods Softw.* 21 (2006) 155–168.
- [10] H.K. Birnbaum, P. Sofronis, Hydrogen-enhanced localized plasticity—a mechanism for hydrogen-related fracture, *Mater. Sci. Eng.: A* 176 (1–2) (1994) 191–202.
- [11] B. Bourdin, G. Francfort, J.-J. Marigo, Numerical experiments in revisited brittle fracture, *J. Mech. Phys. Solids* 48 (4) (2000) 797–826.
- [12] B. Bourdin, G. Francfort, J.-J. Marigo, *The Variational Approach to Fracture*, Springer, Berlin, 2008.
- [13] A. Braides, *Approximation of Free-discontinuity Problems*, Springer Science & Business Media, Berlin, 1998.
- [14] S. del Busto, C. Betegón, E. Martínez-Pañeda, A cohesive zone framework for environmentally assisted fatigue, *Eng. Fract. Mech.* 185 (2017) 210–226.
- [15] A. Díaz, J. Alegre, I. Cuesta, Coupled hydrogen diffusion simulation using a heat transfer analogy, *Int. J. Mech. Sci.* 115 (2016) 360–369.
- [16] R. Falkenberg, A phase field approach to fracture with mass transport extension for the simulation of environmentally-assisted cracking, in: *Key Engineering Materials*, vol. 754, Trans Tech Publ, 2017, pp. 153–156.
- [17] R. Falkenberg, Modelling of environmentally assisted material degradation in the crack phase-field framework, *Proc. Inst. Mech. Eng., Part L: J. Mater.: Des. Appl.* (2018), <https://doi.org/10.1177/1464420718761220>.
- [18] G. Francfort, J.-J. Marigo, Revisiting brittle fracture as an energy minimization problem, *J. Mech. Phys. Solids* 46 (8) (1998) 1319–1342.
- [19] M. Frémond, B. Nedjar, Damage, gradient of damage and principle of virtual power, *Int. J. Solids Struct.* 33 (8) (1996) 1083–1103.
- [20] C. Geuzaine, J.-F. Remacle, Gmsh: a three-dimensional finite element mesh generator with built-in pre- and post-processing facilities, *Int. J. Numer. Eng.* 79 (11) (2009) 1309–1331.
- [21] S. Goswami, C. Anitescu, S. Chakraborty, T. Rabczuk, Transfer learning enhanced physics informed neural network for phase-field modeling of fracture, *Theoret. Appl. Fract. Mech.* 106 (2020) 102447.
- [22] M. Hofacker, C. Miehe, Continuum phase field modeling of dynamic fracture: variational principles and staggered FE implementation, *Int. J. Fract.* 178 (1) (2012) 113–129.
- [23] E. Hondros, M. Seah, The theory of grain boundary segregation in terms of surface adsorption analogues, *Metall. Trans. A* 8 (9) (1977) 1363–1371.
- [24] M. Jirásek, Comparative study on finite elements with embedded discontinuities, *Comput. Methods Appl. Mech. Eng.* 188 (2000) 307–330.
- [25] M. Klinsmann, D. Rosato, M. Kamlah, R.M. McMeeking, An assessment of the phase field formulation for crack growth, *Comput. Methods Appl. Mech. Eng.* 294 (2015) 313–330.
- [26] P.K. Kristensen, E. Martínez-Pañeda, Phase field fracture modelling using quasi-newton methods and a new adaptive step scheme, *Theoret. Appl. Fract. Mech.* (2020) in press.
- [27] P.K. Kristensen, C.F. Niordson, E. Martínez-Pañeda, A phase field model for elastic-gradient-plastic solids undergoing hydrogen embrittlement, *J. Mech. Phys. Solids* 143 (2020) 104093.
- [28] A. Kumar, B. Bourdin, G.A. Francfort, O. Lopez-Pamies, Revisiting nucleation in the phase-field approach to brittle fracture, *J. Mech. Phys. Solids* 142 (2020) 104027.
- [29] S. Lee, M.F. Wheeler, T. Wick, Pressure and fluid-driven fracture propagation in porous media using an adaptive finite element phase field model, *Comput. Methods Appl. Mech. Eng.* 305 (2016) 111–132.
- [30] S.L. Lee, D.J. Unger, A decohesion model of hydrogen assisted cracking, *Eng. Fract. Mech.* 31 (4) (1988) 647–660.
- [31] T. Li, J.-J. Marigo, D. Guilbaud, S. Potapov, Gradient damage modeling of brittle fracture in an explicit dynamics context, *Int. J. Numer. Meth. Eng.* 108 (11) (2016) 1381–1405.
- [32] E. Lorentz, A. Andrieux, A variational formulation for nonlocal damage models, *Int. J. Plas.* 15 (1999) 119–138.
- [33] T.K. Mandal, V.P. Nguyen, J.Y. Wu, Length scale and mesh bias sensitivity of phase-field models for brittle and cohesive fracture, *Eng. Fract. Mech.* 217 (2019) 106532.
- [34] T.K. Mandal, V.P. Nguyen, J.Y. Wu, Evaluation of variational phase-field models for dynamic brittle fracture, *Eng. Fract. Mech.* 235 (2020) 107169.
- [35] T.K. Mandal, V.P. Nguyen, J.-Y. Wu, A length scale insensitive anisotropic phase field fracture model for hyperelastic composites, *Int. J. Mech. Sci.* (105941) (2020).
- [36] T.K. Mandal, V.P. Nguyen, J.Y. Wu, C. Nguyen-Thanh, and A. de Vaucorbeil, *Fracture of thermo-elastic solids: phase-field modelling and new results with an efficient monolithic solver*. under review, 2020.
- [37] E. Martínez-Pañeda, S. del Busto, C.F. Niordson, C. Betegón, Strain gradient plasticity modeling of hydrogen diffusion to the crack tip, *Int. J. Hydrogen Energy* 41 (24) (2016) 10265–10274.
- [38] E. Martínez-Pañeda, A. Golahmar, C.F. Niordson, A phase field formulation for hydrogen assisted cracking, *Comput. Methods Appl. Mech. Eng.* 342 (2018) 742–761.
- [39] E. Martínez-Pañeda, Z.D. Harris, S. Fuentes-Alonso, J.R. Scully, J.T. Burns, On the suitability of slow strain rate tensile testing for assessing hydrogen embrittlement susceptibility, *Corros. Sci.* 163 (2020) 108291.
- [40] C. Miehe, S. Mauthe, Phase field modeling of fracture in multi-physics problems. Part III. Crack driving forces in hydro-poro-elasticity and hydraulic fracturing of fluid-saturated porous media, *Comput. Methods Appl. Mech. Eng.* 304 (2016) 619–655.
- [41] C. Miehe, L.-M. Schänzel, Phase field modeling of fracture in rubbery polymers. Part I: Finite elasticity coupled with brittle failure, *J. Mech. Phys. Solids* 65 (2014) 93–113.
- [42] C. Miehe, M. Hofacker, F. Welschinger, A phase field model for rate-independent crack propagation: robust algorithmic implementation based on operator splits, *Comput. Methods Appl. Mech. Eng.* 199 (45–48) (2010) 2765–2778.
- [43] C. Miehe, M. Hofacker, L.-M. Schänzel, F. Aldakheel, Phase field modeling of fracture in multi-physics problems. Part II. Coupled brittle-to-ductile failure criteria and crack propagation in thermo-elastic-plastic solids, *Comput. Methods Appl. Mech. Eng.* 294 (2015) 486–522.
- [44] C. Miehe, L.-M. Schänzel, H. Ulmer, Phase field modeling of fracture in multi-physics problems. Part I. Balance of crack surface and failure criteria for brittle crack propagation in thermo-elastic solids, *Comput. Methods Appl. Mech. Eng.* 294 (2015) 449–485.
- [45] N. Moës, J. Dolbow, T. Belytschko, A finite element method for crack growth without remeshing, *Int. J. Numer. Meth. Eng.* 46 (1) (1999) 133–150.
- [46] V.P. Nguyen, J.Y. Wu, Modeling dynamic fracture of solids using a phase-field regularized cohesive zone model, *Comput. Methods Appl. Mech. Eng.* 340 (2018) 1000–1022.
- [47] V.P. Nguyen, C.T. Nguyen, S. Bordes, A. Heidapour, Modelling interfacial cracking with non-matching cohesive interface elements, *Comput. Mech.* 58 (5) (2016) 731–746.
- [48] C. Nguyen-Thanh, V.P. Nguyen, A. de Vaucorbeil, T.K. Mandal, J.-Y. Wu, Jive: an open source, research-oriented c++ library for solving partial differential equations, *Adv. Eng. Softw.* (2020) under review.
- [49] K. Pham, H. Amor, J.-J. Marigo, C. Maurini, Gradient damage models and their use to approximate brittle fracture, *Int. J. Damage Mech.* 20 (2011) 618–652.
- [50] K.H. Pham, K. Ravi-Chandar, The formation and growth of echelon cracks in brittle materials, *Int. J. Fract.* 206 (2) (2017) 229–244.
- [51] T. Rabczuk, T. Belytschko, Cracking particles: a simplified meshfree method for arbitrary evolving cracks, *Int. J. Numer. Meth. Eng.* 61 (13) (2004) 2316–2343.
- [52] N. Raykar, S. Maiti, R.S. Raman, S. Aryan, Study of hydrogen concentration dependent growth of external annular crack in round tensile specimen using cohesive zone model, *Eng. Fract. Mech.* 106 (2013) 49–66.
- [53] H. Ren, X. Zhuang, Y. Cai, T. Rabczuk, Dual-horizon peridynamics, *Int. J. Numer. Meth. Eng.* 108 (12) (2016) 1451–1476.
- [54] E. Samaniego, C. Anitescu, S. Goswami, V.M. Nguyen-Thanh, H. Guo, K. Hamdia, X. Zhuang, T. Rabczuk, An energy approach to the solution of partial differential equations in computational mechanics via machine learning: concepts, implementation and applications, *Comput. Methods Appl. Mech. Eng.* 362 (2020) 112790.
- [55] I. Scheider, M. Pffuff, W. Dietzel, Simulation of hydrogen assisted stress corrosion cracking using the cohesive model, *Eng. Fract. Mech.* 75 (15) (2008) 4283–4291.
- [56] I. Scheider, M. Pffuff, W. Dietzel, Simulation of hydrogen assisted stress corrosion cracking using the cohesive model, *Eng. Fract. Mech.* 75 (15) (2008) 4283–4291.
- [57] A. Schlüter, A. Willenbücher, C. Kuhn, R. Müller, Phase field approximation of dynamic brittle fracture, *Comput. Mech.* 54 (5) (2014) 1141–1161.
- [58] S. Serebrinsky, E. Carter, M. Ortiz, A quantum-mechanically informed continuum model of hydrogen embrittlement, *J. Mech. Phys. Solids* 52 (10) (2004) 2403–2430.
- [59] J. Simó, J. Oliver, F. Armero, An analysis of strong discontinuities induced by strain-softening in rate-independent inelastic solids, *Comput. Mech.* 12 (1993) 277–296.
- [60] P. Sofronis, R. McMeeking, Numerical analysis of hydrogen transport near a blunting crack tip, *J. Mech. Phys. Solids* 37 (3) (1989) 317–350.
- [61] E. Tanné, T. Li, B. Bourdin, J.-J. Marigo, C. Maurini, Crack nucleation in variational phase-field models of brittle fracture, *J. Mech. Phys. Solids* 110 (2018) 80–99.

- [62] G.N. Wells, L.J. Sluys, A new method for modelling cohesive cracks using finite elements, *Int. J. Numer. Meth. Eng.* 50 (12) (2001) 2667–2682.
- [63] J.Y. Wu, A unified phase-field theory for the mechanics of damage and quasi-brittle failure in solids, *J. Mech. Phys. Solids* 103 (2017) 72–99.
- [64] J.Y. Wu, A geometrically regularized gradient-damage model with energetic equivalence, *Comput. Methods Appl. Mech. Eng.* 328 (2018) 612–637.
- [65] J.Y. Wu, Numerical implementation of non-standard phase-field damage models, *Comput. Methods Appl. Mech. Eng.* 340 (2018) 767–797.
- [66] J.Y. Wu, Y. Huang, Comprehensive implementations of phase-field damage models in abaqus, *Theoret. Appl. Fract. Mech.* 106 (2020) 102440.
- [67] J.Y. Wu, F.B. Li, An improved stable xfem (is-xfem) with a novel enrichment function for the computational modeling of cohesive cracks, *Comput. Methods Appl. Mech. Eng.* 295 (2015) 77–107.
- [68] J.Y. Wu, V.P. Nguyen, A length scale insensitive phase-field damage model for brittle fracture, *J. Mech. Phys. Solids* 119 (2018) 20–42.
- [69] J.Y. Wu, F.B. Li, S.L. Xu, Extended embedded finite elements with continuous displacement jumps for the modeling of localized failure in solids, *Comput. Methods Appl. Mech. Eng.* 285 (2015) 346–378.
- [70] J.Y. Wu, V.P. Nguyen, C.T. Nguyen, D. Sutula, S. Sinaie, S. Bordas, Phase field modeling of fracture, *Adv. Appl. Mech.: Fract. Mech.: Recent Develop. Trends* 53 (2019), doi: 10.1016/bs.aams.2019.08.001, in press.
- [71] J.Y. Wu, Y. Huang, V.P. Nguyen, On the bfgs monolithic algorithm for the unified phase field damage theory, *Comput. Methods Appl. Mech. Eng.* (2020) 112704.
- [72] J.Y. Wu, T.K. Mandal, V.P. Nguyen, A phase-field regularized cohesive zone model for hydrogen assisted cracking, *Comput. Methods Appl. Mech. Eng.* 358 (112614) (2020).
- [73] X. Xu, A. Needleman, Numerical simulations of fast crack growth in brittle solids, *J. Mech. Phys. Solids* 42 (9) (1994).
- [74] S. Zhou, X. Zhuang, T. Rabczuk, A phase-field modeling approach of fracture propagation in poroelastic media, *Eng. Geol.* 240 (2018) 189–203.